University of Basel
Institute of Physics

Master's Thesis

Conductance Fluctuations in Molecular Junctions

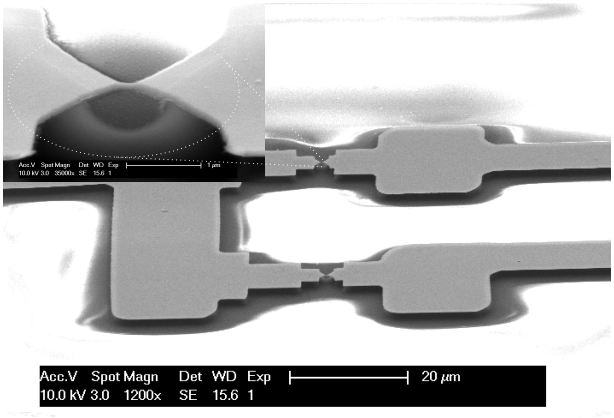

Jan Brunner
Therwil

February, 2009

Supervisors:
Dr. Michel Calame
Prof. Christian Schönenberger

Mechanically controllable break junctions have been used to investigate the conductance fluctuations in different gold-molecule-gold junctions. Alkanes and oligo(phenylene ethynylene) (OPE) molecules with thiol linker groups as well as OPE with pyridine linker groups have been investigated. The main focus was on the characterization of random telegraph signals (RTS) that were observed while the distance between the two gold electrodes was not actively changed. We find that these signals show a broad range of relative amplitudes (typically from 0.2 to 5) and state lifetimes (typically from 10^{-4} to 10^{-1} s). We obtain evidence that the properties of the observed RTS depend on the molecular compound inserted in the junction.

Contents

1 Introduction

Ever since the invention of the transistor and integrated circuits, their feature sizes have been continuously reduced. Although traditional top-down techniques still have room for improvement, fundamental or technical limits preventing smaller feature size might be encountered sooner or later. Possible alternatives are bottom-up techniques like molecular electronics. A major requirement in research and later applications of molecular electronics are stable electrical contacts to individual molecules. It has been shown that good mechanical stability of the electrodes used to contact molecules is necessary in order to get long lifetimes of the molecule–metal bonds. In vacuum, junction lifetimes of several hours have been reached at room temperature with mechanically controllable break junctions [1]. Despite some practical success with contacting molecules, the atomic arrangement of and processes in molecular junctions is still a matter of debate. In this work, mechanically controllable break junctions are used to investigate conductance fluctuations observed in liquid at room temperature. From the fluctuations, some insight into the microscopic properties of molecular junctions can be gained.

1.1 Measurement Setup

1.1.1 Mechanically Controllable Break Junction Principle

Mechanically controllable break junctions (MCBJ) consist of conductive leads on a flexible and non-conductive or insulated substrate. In this work, the samples were prepared as follows: Spring steel with a thickness of 0.3 mm was covered by a polyimide insulation layer. Gold leads were prepared by electron beam lithography and vapor coating (60 nm gold on 10 nm titanium for adhesion). The samples were then exposed to a oxygen/CHF_3 plasma which etches the polyimide, leaving free-standing gold bridges of typical length $U \approx 500\,\mathrm{nm}$ (figure 1.1).

In the measurement apparatus (figure 1.2), the sample is held between two counter-supports from the top and a push rod from below. It is bent by moving up the push rod which is located below the free-standing gold bridge. The bending stretches the gold bridge which eventually breaks, forming two gold electrodes. Their separation d then depends approximately linearly on the push rod position z with an estimated attenuation factor $a = \Delta d/\Delta z$ in between $1.6 \cdot 10^{-5}$ and $4 \cdot 10^{-5}$ [2]. This low attenuation factor allows for a fine adjustment of the electrode separation and leads to a low sensitivity to vibrations.

For measurements in liquid, a liquid cell is pressed onto the sample and filled with a solvent or solution of molecules. A short piece of flexible Viton tube between the sample and the rigid part of the liquid cell seals the gap.

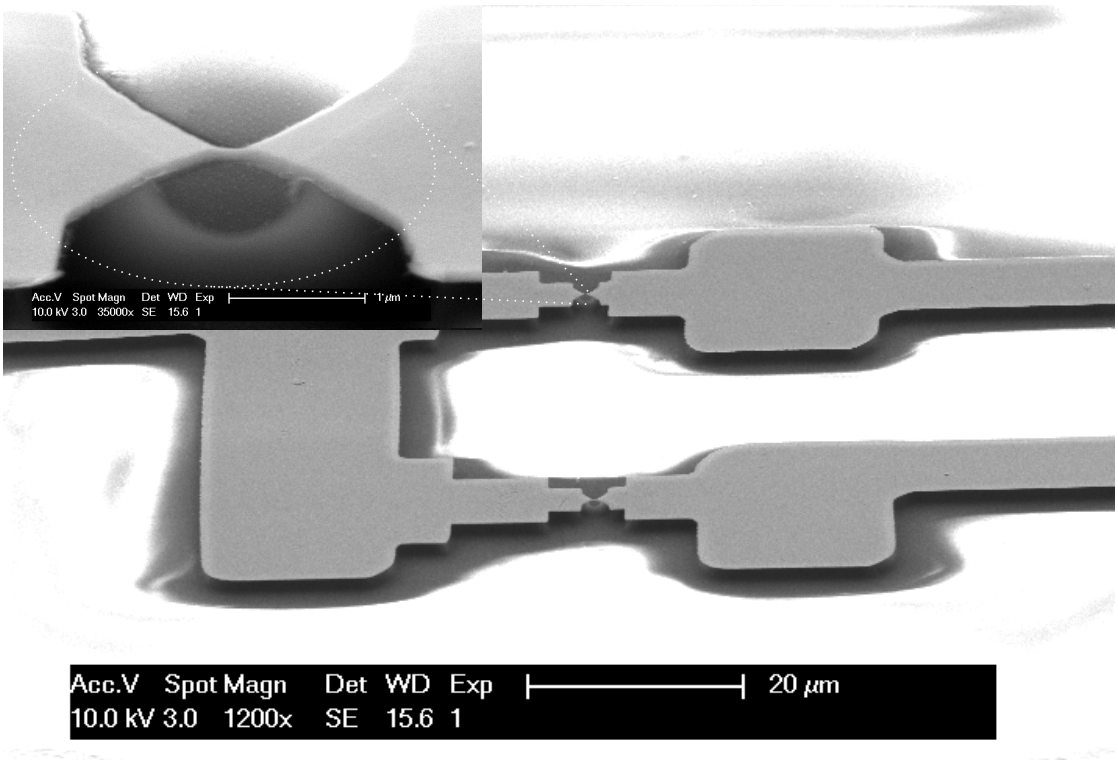

FIGURE 1.1: SEM picture of the central region of a typical sample. Two free-standing gold bridges are visible.

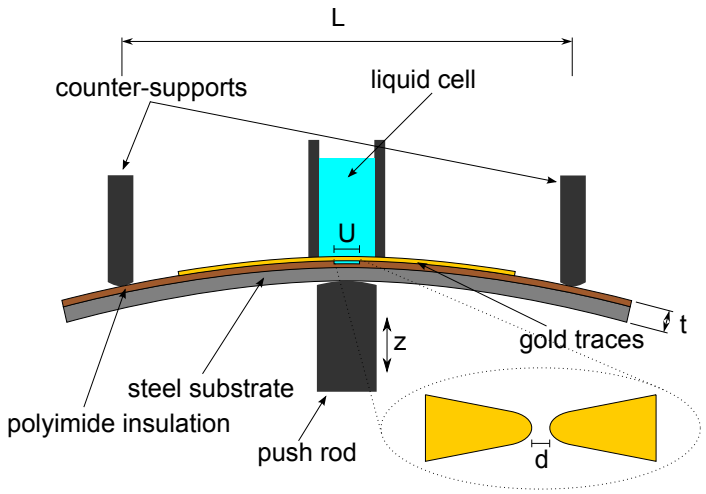

FIGURE 1.2: Sketch of the mechanically controllable break junction setup for measurements in liquid. The free-standing gold bridge of length U is stretched by moving the push rod which presses against the middle of the sample of thickness t, adjusting the electrode separation d. The counter-supports are separated by $L = 20\,\mathrm{mm}$.

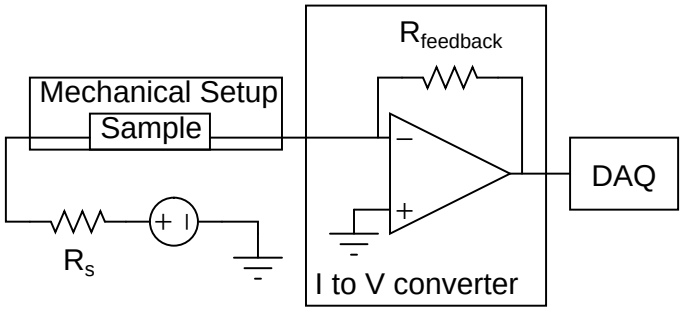

FIGURE 1.3: Schematic of the electronic setup. A voltage source of 0.2 V is connected to one contact of a break junction (installed in the mechanical setup) while the input of an I/V converter is connected to the other contact. The output voltage of the I/V converter is measured by a data acquisition board (DAQ) and recorded on a computer.

1.1.2 Electronics

A schematic of the electronic setup is shown in figure 1.3. One of the two contacts of a break junction is connected to a voltage source of 0.2 V, the other contact to the input of an auto ranging I to V converter with four gain settings from 10^4 to 10^9 V/A. The output voltage of the converter is measured by a National Instruments data acquisition board. A series resistance of 1 kΩ limits the current allowed to run through the sample. The whole mechanical setup is enclosed in an aluminum box and all cables entering it are shielded. Care has been taken to avoid ground loops. Typical current fluctuations at the highest gain setting with the junction fully open are in the order of $\pm 2.5 \cdot 10^{-12}$ A which translates to apparent conductance fluctuations of $\approx 1.5 \cdot 10^{-7} G_0$ with the used bias voltage.

2 Conductance of Molecules

2.1 Measurement Technique

The conductance of molecules was measured by doing repeated cycles of opening and closing of the junction while the conductance was being recorded. During opening, the push rod moves up until the conductance falls below a low threshold value close to the detection limit. During closing, the push rod moves down until a defined high conductance value is passed. This high conductance value can be either greater than G_0 (typically 9 to 30 G_0, "contact mode") or smaller than G_0 (typically 0.01 G_0, "non-contact mode"). We will first focus on contact mode measurements. The push rod was moved at a typical speed of 31.2 µm/s while the conductance was recorded at a sampling rate of 500 Hz.

While the junction is being opened with no gold-binding molecules present, its conductance steadily decreases at first as the gold bridge is getting narrower (Ohm's law). At lower conductance values, the junction behaves ballistically, preferentially taking conductance values close to integer multiples of the quantum of conductance ($G_0 = \frac{2e^2}{h} = (12.9\,\mathrm{k\Omega})^{-1}$) decreasing stepwise down to 1 G_0 where the junction is just one gold atom wide. In this region, conductance plateaus are observed (constant conductance while the push rod is moved). After further movement, the gold bridge breaks and the electrodes quickly separate by a few Å because of mechanical relaxation which causes the conductance to jump down to between 10^{-2} and $10^{-4}\,G_0$ (tunneling regime). Further separation leads to an exponential decrease of the tunneling conductance ($G \propto e^{-\beta d}$) until the detection limit is reached.

If the opening and closing cycles are performed with the junction in a solution of molecules capable of binding to gold, the observed conductance traces can show additional plateaus in the tunneling regime that correspond to situations where the electrode gap is bridged by one or more molecules. The measured molecules are thought to be bound to both sides of the junction before the breaking event in most cases (figure 2.1). When molecules bridge the gap while the junction is opening, they prevent the electrodes from separating further, leading to conductance plateaus. During a plateau, further stress of the opening motion is accommodated by plastically or elastically deforming the gold tips. This mechanism of plateau formation works regardless of the conductance of the molecules.

The conductance traces differ from each other due to different atomical arrangements and random processes. To get reproducible conductance values it is therefore necessary to statistically analyze many cycles. For this reason, histograms of the recorded opening conductance traces were calculated as proposed by González et al [2]. Peaks in those histograms correspond to conductance values preferentially taken by the junction.

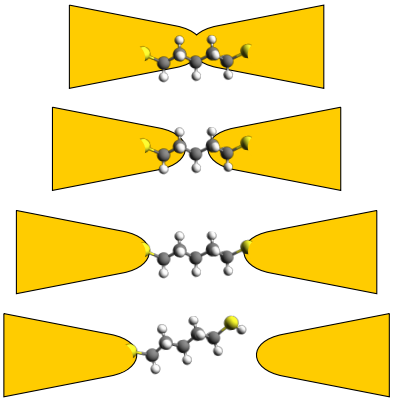

FIGURE 2.1: Probable mechanism of plateau formation: The molecule is already bound to both gold electrodes when they are still in contact with each other (top). The electrodes separate with the molecule still bound to both of them and separate further until the molecule has slid to the apexes and is stretched. Now the molecule prevents the electrode tips from separating further until one of the molecule–electrode bonds breaks.

2.2 Alkanes

Alkanes are simple molecules which are often used as reference in molecular electronics experiments [2, 3]. Measurements have been performed as described above both with pure mesitylene and with solutions of 1 mM alkanedithiols in mesitylene. Thiol groups (-SH) are known to covalently bind to gold surfaces. It is therefore expected that alkanedithiols are able to bridge a small gap between the gold electrodes to form a metal–molecule–metal junction. Alkanedithiols with 5, 6, 8 and 9 carbon atoms were investigated in contact mode.

Looking at opening conductance curves obtained with mesitylene (figure 2.2), we see the aforementioned sudden conductance decrease caused by electrode relaxation followed by an exponential decay down to the detection limit. A logarithmic histogram of the conductance values of those opening curves (figure 2.3) shows peaks around 1 and $2\,G_0$ but is otherwise approximately flat due to the exponential tunneling decay. There are slightly lower counts between 1 and $10^{-4}\,G_0$ because of the electrode separation jump.

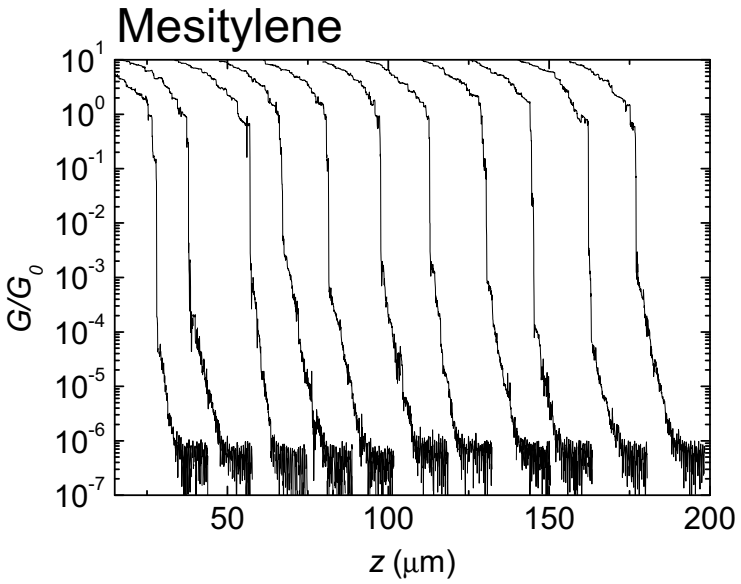

FIGURE 2.2: Typical opening conductance traces obtained with pure mesitylene. After breaking at $\approx 1\,G_0$ and the following drop by 2 to 4 orders of magnitude, an exponential decay of the conductance is observed.

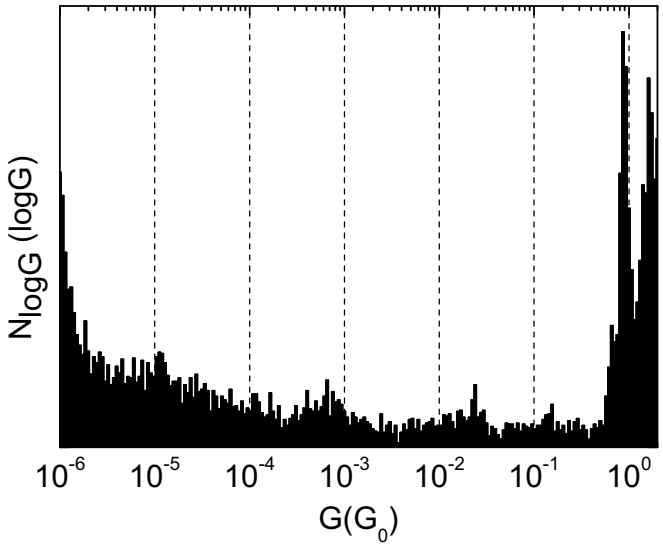

FIGURE 2.3: Histogram of 50 consecutive opening curves in mesitylene. Apart from the 1 and $2\,G_0$ peaks, only a flat tunneling background is seen.

If the same measurement is performed with alkanedithiol solutions instead of pure mesitylene, additional plateaus are observed in the opening traces (figure 2.4). Figure 2.5 shows typical logarithmic conductance histograms of 100 consecutive opening curves per molecule. It can be seen that pentanedithiol (C5) and hexanedithiol (C6) give less well-defined histogram peaks than octanedithiol (C8) and nonanedithiol (C9) with C5 being quite hard to discern in some measurements. Individual C5 curves often show no or short plateaus.

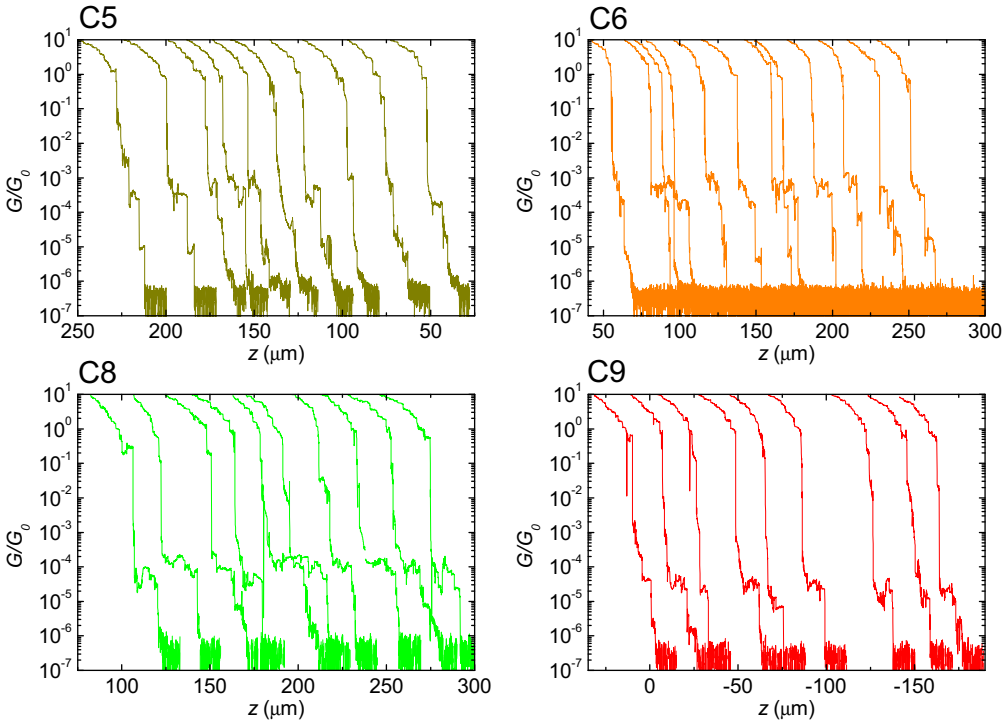

FIGURE 2.4: Typical opening conductance curves obtained in alkanedithiol solutions. Stable plateaus in the tunneling regime are observed in most curves for C8 and C9 whereas C5 and C6 curves show less stable, shorter plateaus.

Table 2.1 shows conductance values for different molecules obtained as follows. A Gaussian fit to the logarithmic histogram leads to peak center g_c and distribution width w_g. From those values, the peak positions G_c in the linear scale are obtained according to Huber et al, $\log(G_c) = g_c \ln(10) w_g^2$ [4]. The values $G_A \equiv G_c$ are shown in table 2.1 where G_{min} and G_{max} indicate the distribution range observed in the log histogram (68 % confidence interval). Note that this range corresponds to the spread during a single measurement which is caused by different realization of the molecular junction during each cycle.

Figure 2.6 shows the obtained conductance values plotted against the number n_C of carbon atoms in the alkane chain of the corresponding molecules. A linear fit of

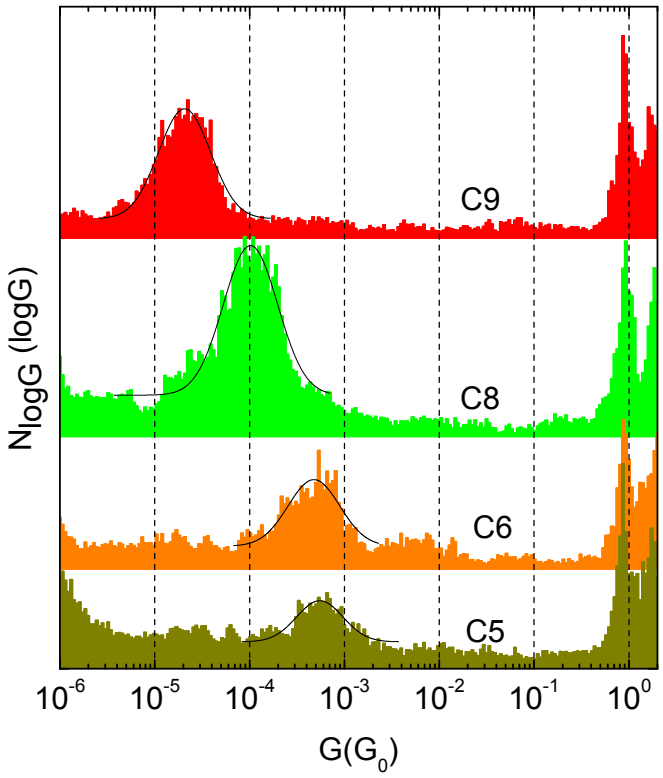

FIGURE 2.5: Logarithmic conductance histograms of C9, C8, C6 and C5. 100 consecutive opening curves were used for each molecule. The bin size was 0.03 $\log(G/G_0)$. The Gaussian functions fitted to the histogram peaks are shown in black.

the values transformed to a semi-log scale (equation 2.1) leads to a tunneling decay constant per carbon of $\beta_N = 0.83 \pm 0.15$ and a resistance extrapolated to $n_C = 0$ of $(367 + 716/ - 242)\,\mathrm{k}\Omega$. The obtained decay constant is in agreement with the $\beta_N = 0.92 \pm 0.19$ averaged from experiments using different methods (STM, conductive AFM, Hg drop, nano pores, large area junctions, etc.) by Akkerman et al [3].

The fit with the values obtained from 100 curves per molecule is not very accurate and suggests a non-exponential relation. When using more curves for the histograms, the exponential decay fits better but it is still not certain whether the slopes at low and high n_C are the same (see section B.1 for the additional data). As the measurements in C5 and C6 more often show short or no plateaus in comparison to C8 and C9, the plateau formation mechanism might be different for the short molecules. This different mechanism could lead to different favored conductance values.

Molecule	G_A $(10^{-5}\,G_0)$	G_{min} $(10^{-5}\,G_0)$	G_{max} $(10^{-5}\,G_0)$
C5	40	31	97
C6	32	25	89
C8	6.6	5.3	20
C9	1.4	1.1	3.9

TABLE 2.1: Conductance values of alkanedithiols. G_A are the most probable values, G_{min} and G_{max} indicate the boundaries of the 68 % confidence intervals.

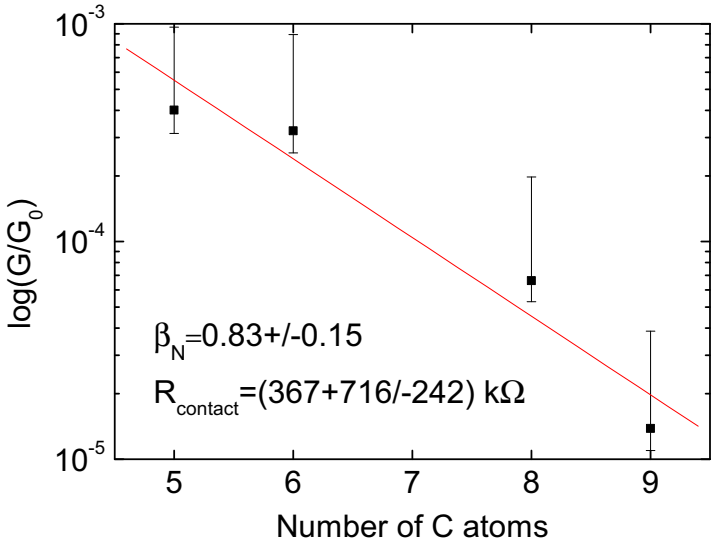

FIGURE 2.6: Plot of the conductance values from table 2.1. The linear fit to the logarithms of the conductance values leads to a tunneling decay constant $\beta_N = 0.83 \pm 0.15$ (per carbon) and an extrapolated resistance of $(367 + 716/ - 242)$ kΩ for zero C atoms. The error bars represent the 68 % confidence intervals obtained in the log scale.

$$G = G_0 \cdot e^A \cdot e^{-\beta_N n_c} \Rightarrow \ln \frac{G}{G_0} = A - \beta_N \cdot n_C \tag{2.1}$$

2.2.1 Discussion

C5 and C6 measurements show considerably less well-defined plateaus than their longer counterparts but the molecule peaks are still visible in the histograms. This is in slight contrast to published results of other groups who don't see conductance trough alkanedithiols with less than six carbon atoms when doing cycles with forced gold-gold contacts, for example Huisman et al [5]. Measurements with 1,4-benzenedithiol, another short dithiol molecule, showed broad conductance peaks with a low number of histogram counts [6, 7]. This confirms the observation that short dithiol molecules are particularly

hard to characterize by doing open/close cycles with break junctions. On the other hand, Venkataraman et al see qualitatively similar conductance curves and histograms for all diaminoalkanes from 12 down to 2 carbon atoms, each showing well-defined plateaus and histogram peaks [7, 8]. It seems therefore that short molecules with amine linker groups can easily be measured as opposed to those with thiol linker groups. This raises the question which properties of the two linker groups (thiols and amines) are responsible for the different behavior and motivates further experiments with different linker groups.

Huisman et al explain the lack of plateaus with short thiol molecules as follows: Before the gold electrodes are jumping out of contact to an estimated gap size of 2.5 to 5 Å, the molecules are already bound to both electrodes. Whereas long molecules are most likely in a bent conformation and able to deform in response to the distance jump, short molecules are most probably already stretched and unable to elongate sufficiently to bridge the newly formed gap, losing contact to one of the electrodes [5]. The molecules are 8 Å (C5) to 13 Å (C9) long (S–S distance).

It is estimated from measurements and simulations that the bond energies $E_{Au-S} > E_{Au-Au} > E_{Au-N}$ and also that the forces necessary to break the bonds $F_{Au-S} > F_{Au-Au} > F_{Au-N}$ [8, 9]. Therefore the molecular bridge is expected to break between gold and nitrogen for amine linker groups but between two gold atoms for thiols. Taking this into account, one would expect that jumping out of contact of the electrodes causes molecular junctions with short molecules to break regardless of the linker groups. One quality that could prevent the breaking is the ability of the linker group to easily slide on the electrode's surface. It could also be that the kinetic properties of the bond formation are quicker for Au–N than for Au–Au, allowing the bond to reform immediately after breaking.

At the moment, it is unclear which of the possible explanations is true. Studies of the microscopic behavior of the junctions (thermal fluctuations, kinetics) might give answers.

2.3 Different conductance values when not closing to contact

So far, we have only looked at cycles where the junction was fully closed to conductance values well above $1\,G_0$ before opening again ("contact mode"). When the junction was not closed to contact but only until a conductance threshold of $10^{-2}\,G_0$ was reached ("non-contact mode"), we observe peaks at new positions in the conductance histograms of C8 as shown in figure 2.7. Peaks show up between 10^{-4} and $10^{-3}\,G_0$ in non-contact mode whereas there is no peak in this conductance range in contact mode.

More thorough measurements [10] show a mean conductance value of $G_A = 4.5 \pm 1.1 \times 10^{-5}\,G_0$ for contact mode, confirming previously known values from MCBJ measurements. For non-contact measurements, linear histograms show a peak at $G_B = 2.3 \pm 0.3 \times 10^{-4}\,G_0$. Values close to this have previously been measured in STM experiments by Xu et al [11] (closing threshold unknown) and Li et al [12] (non-contact mode). In both contact and non-contact mode measurements, conductance peaks at $G_C = 1.2 \times 10^{-5}\,G_0$ and integer multiples nG_C (n=1, 2) were observed (but clearer in

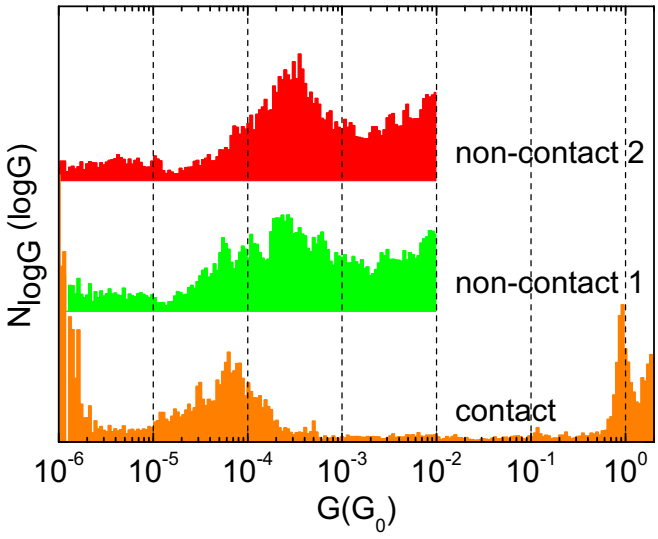

FIGURE 2.7: Three logarithmic conductance histograms calculated from sets of 50 (contact and non-contact 1) or 25 (non-contact 2) opening curves of the same sample in C8 solution. In contact mode (green), the junction was closed to $G > 10\,G_0$ in each cycle whereas the motor was stopped at $G = 10^{-2}\,G_0$ in non-contact mode. In contact mode, a broad peak around the known conductance value of $4.5 \cdot 10^{-5}\,G_0$ is seen with no features visible above $10^{-4}\,G_0$. In non-contact mode, new peaks appear between 10^{-4} and $10^{-3}\,G_0$.

contact mode). As there are no clear multiples of the G_A and G_B, G_C seems to be the best candidate for single-molecule conductance. G_A is presumed to be the conductance of the most favored microscopic arrangement in contact mode with a few molecules bridging the gap in parallel. In non-contact mode, we expect the electrode tips to become more blunt because of relaxation and mechanical deformation which would allow even more molecules in parallel to bridge the gap, possibly explaining G_B.

2.4 Oligo(phenylene ethynylene) molecules

Molecules containing conjugated structures are of particular interest for molecular electronics as their HOMO–LUMO gap is less than that of saturated molecules, leading to a higher conductance for the same length. Also, the linker groups of a molecule are expected to have a strong influence on the measured conductance and the stability of the formed molecular junctions, motivating their study.

As examples of conjugated molecules, three variants of Oligo(phenylene ethynylene) (OPE) with different linker groups were measured in contact mode. The linker groups of the OPE molecules investigated were either two thiols (S-OPE-S), two pyridines (N-OPE-N) or a single thiol group (S-OPE-H) (see figure 2.8 for the chemical structures). To prevent polymerization or dimerization, the thiol groups were protected by acetyl

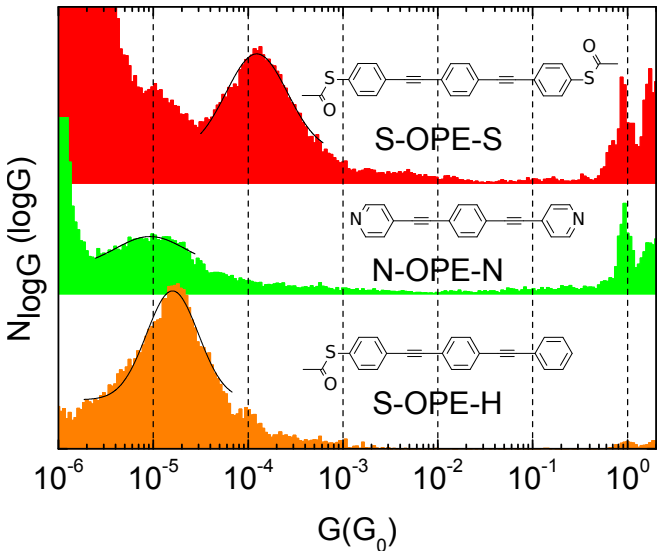

FIGURE 2.8: Logarithmic histograms of the opening curves of OPE molecules with two thiol groups (top, 100 cycles), two pyridine groups (middle, 100 cycles) and a single thiol group (bottom, 45 cycles).

Molecule	G_A ($10^{-5}\,G_0$)	G_{min} ($10^{-5}\,G_0$)	G_{max} ($10^{-5}\,G_0$)
S-OPE-S	7.1	5.9	26
N-OPE-N	0.45	0.39	2.1
S-OPE-H	1.1	0.85	3.0

TABLE 2.2: Conductance values of OPE molecules. G_A are the most probable values, G_{min} and G_{max} indicate the boundaries of the 68 % confidence intervals.

groups before measuring. 0.25 mM of the molecules were dissolved in a 1:4 mixture of tetrahydrofuran (THF) and mesitylene and roughly 1 ml of these solutions were put into the liquid cell for measurements. The protection groups of the thiol molecules were removed in situ by adding $\sim 100\,\mu$M of tetrabutylammonium hydroxide (TBAH) to the solution. The solution was continuously bubbled with argon to prevent thiol oxidation. Figure 2.8 shows logarithmic histograms of opening curves of S-OPE-S, N-OPE-N and S-OPE-H (from top to bottom). The conductance values (table 2.2) were obtained as in the alkanedithiols case.

We note that the N-OPE-N histogram shows a less pronounced peak at a lower conductance than S-OPE-S even though the molecule is slightly shorter. The nitrogen of the pyridine is thought to form a donor–acceptor bond to a gold atom, similar to the nitrogen of primary amine groups [8]. This donor–acceptor bond leads to weaker coupling of the molecule to the gold as compared to the thiol case. In contrast, S-OPE-H shows a well-defined peak with a statistical weight similar to the S-OPE-S case. The surprising finding that aromatic molecules with only one linker group can reliably bridge the electrode gap has been attributed to π–π stacking [13]. These π–π interactions might also have an effect on the stability of the sulfur–gold bond. For this reason, the OPE molecules are interesting candidates for conductance fluctuation measurements (following sections).

3 Conductance Fluctuations

In chapter 2 the conductance of molecules was investigated by looking at conductance curves obtained while cyclicly opening and closing the junction. Now, the focus is set on conductance fluctuations which take place while the electrodes are not actively being moved.

To get an idea of the amplitude of those fluctuations, conductance traces of break junction samples in liquid were obtained as follows. Before a measurement was started, the junction was completely open (conductance below the detection limit). It was then slowly closed to a defined low conductance (usually $10^{-5}\,G_0$) after which the motor was stopped and the recording was automatically started. The push rod was now in a fixed position during a dwelling period of 30 s while the conductance was recorded at 50 Hz sampling rate. After the dwelling period, the junction was closed further by a small step ($\Delta z = 0.2\,\mu\text{m}$) and another dwelling and recording period was immediately started. This cycle continued until a higher conductance threshold (usually $10^{-3}\,G_0$) was reached and the measurement was ended. Both pure mesitylene and 0.1 mM octanedithiol (C8) solution in mesitylene were investigated.

Figure 3.1 shows one representative measurement in mesitylene acquired according to the described procedure. (a) shows the complete conductance trace as a function of time. The vertical gray lines indicate downwards moving of the push rod by $\Delta z = 0.2\,\mu\text{m}$. (b) shows a selection of single 30 second periods of the same measurement in a logarithmic conductance scale. Figure 3.2 shows a measurement with C8 solution.

Looking at the conductance traces ((a) in figures 3.1 and 3.2), we notice an approximately exponential increase with decreasing pushrod height. We also see that the amplitude of fluctuations in the log scale does not change considerably for mesitylene but does so for C8 solution. In both measurements there are phases where the conductance oscillates between two or few values but the amplitudes of such oscillations are larger with C8. In section 3.1, we will further analyze data obtained in this way.

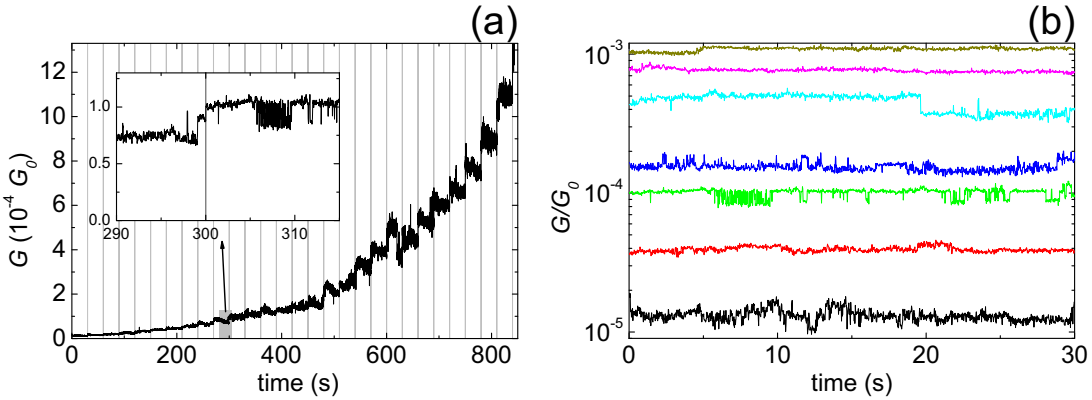

FIGURE 3.1: (a) Conductance trace measured in pure mesitylene. Grey lines indicate active movement steps of $\Delta z = 0.2\,\mu\text{m}$. (b) Selection of single 30 second periods of the same measurement in logarithmic scale.

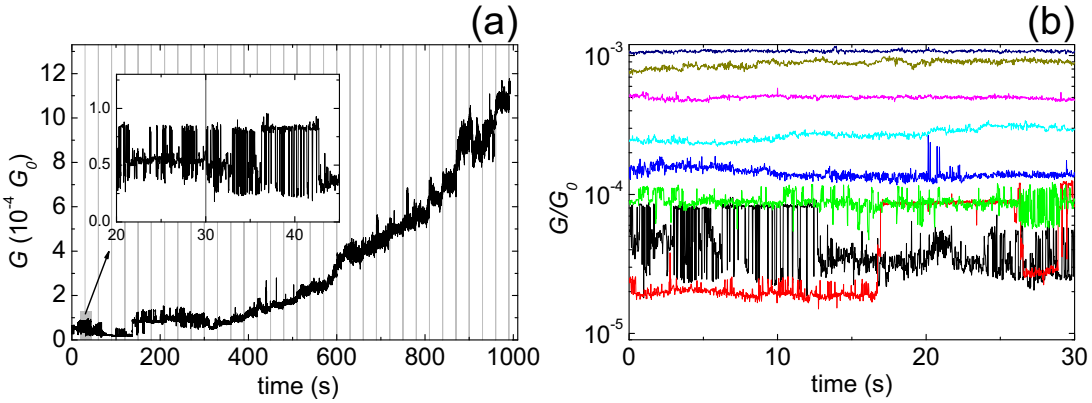

FIGURE 3.2: (a) Conductance trace measured in C8 solution. Grey lines indicate active movement steps of $\Delta z = 0.2\,\mu\text{m}$. (b) Selection of single 30 second periods of the same measurement in logarithmic scale.

3.1 Amplitude of Conductance Fluctuations

The amplitude of fluctuations of $\log G$ seems to be approximately independent of G in the mesitylene measurement. To check for a possible dependence, the standard deviation (defined as in equation 3.1) $\delta \log G \equiv \sigma_{\log G/G_0}$ of $\log G$ was calculated for each 30 s recording period as a measure of fluctuation amplitude. This standard deviation of the logarithm is proportional to the relative standard deviation of the conductance $\frac{\delta G}{\langle G \rangle}$: $\delta \log G = \frac{\delta G}{\langle G \rangle} \cdot \frac{1}{\ln 10}$, $\delta G \ll \langle G \rangle$ (see section A.1 for a derivation).

$$\sigma_x \equiv \sqrt{\left\langle (x_i - \bar{x})^2 \right\rangle} \tag{3.1}$$

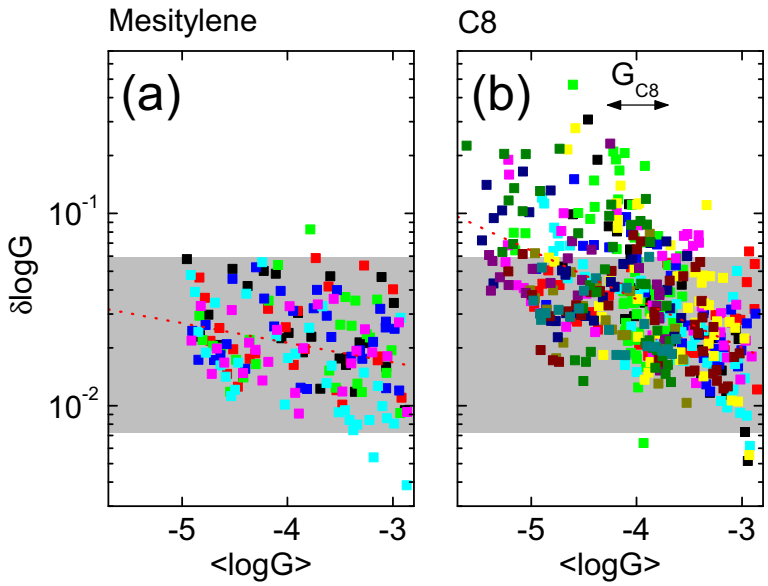

FIGURE 3.3: Representative scatter plots of $\delta \log G$ vs. $\langle \log G \rangle$ for each 30 s dwelling period of 6 measurements shown in different colors in mesitylene (a) and 13 measurements in C8 solution (b) (one sample per plot). The $\delta \log G$ values are spread over one order of magnitude with mesitylene and decrease only slightly with increasing $\langle \log G \rangle$ with a slope of 0.10. With C8 solution, a clearer dependence on $\langle \log G \rangle$ can be seen with a slope of 0.25. The gray areas indicate the observed range with mesitylene (95 % confidence interval). It is also shown in the C8 plot to highlight the difference. The arrow indicates the C8 conductance range (68 % confidence interval) as obtained from opening curves (section 2.2).

Figure 3.3 shows scatter plots of the fluctuation amplitude $\delta \log G$ in relationship to the average $\langle \log G \rangle$ for each 30 s dwelling period. Each measurement is shown in one color. In figure 3.3(a), measured with one sample in pure mesitylene, we observe little dependence of $\delta \log G$ on $\langle \log G \rangle$ and no values higher than 10^{-1}.

It is possible to explain this observation by assuming the conductance to be dominated by tunneling [14] and the fluctuations being caused by thermal movement of the electrode

atoms. The tunneling conductance is of the form $G(d) = C \cdot \exp(-d\beta)$ with d denoting the distance between electrodes and $\beta = 2\sqrt{2m\phi}/\hbar$ the tunneling decay constant which depends on the electron mass m and the effective barrier height ϕ (approximately 3.5 eV for gold in organic solvents). The prefactor C is proportional to the area contributing to the tunneling.

If we assume $\beta = 1\,\text{Å}^{-1}$, we get $\delta d = 0.05\,\text{Å}$ for $\delta \log G = \frac{\delta G}{\langle G \rangle} \frac{1}{\ln 10} = 0.02$ (logarithmic average of the measurement in figure 3.3(a)). This is less than expected as the gold atoms (diameter $\approx 3\,\text{Å}$) are known to be quite mobile at room temperature. The measurement shows approximately no dependence of $\delta \log G$ on $\langle G \rangle$ as expected. Note that we cannot expect to measure the full fluctuation amplitude because of the limited bandwidth of the setup. The real microscopic fluctuations (and therefore δd) are larger than the above estimation.

In the C8 measurement (figure 3.3(b)), the fluctuation amplitudes are significantly higher at low conductance. Also, a clear dependence of $\delta \log G$ on $\langle \log G \rangle$ can be seen. If we fit a straight line to $\log(\delta \log G)$ vs. $\langle \log G \rangle$ (corresponding to a relation $\delta \log G \propto \langle G \rangle^{-\gamma}$), we get an average slope of $\gamma = 0.14 \pm 0.04$ for mesitylene (2 samples, 8 measurements) and $\gamma = 0.23 \pm 0.03$ for C8 (5 samples, 41 measurements). Note that we don't claim that this power relationship has a physical meaning. It is introduced as a measure for the observed dependence. At conductance values above the known C8 junction conductance obtained in section 2.2 (the black arrow indicates the range), the observed amplitudes are as low as in the mesitylene case. See table B.1 for the slopes and average amplitudes of individual samples.

We can conclude that part of the observed fluctuations occur independently of gold-binding molecules and are probably mainly caused by thermal motion of the electrodes as they occur in both pure mesitylene and C8 solution. The large-amplitude fluctuations with $\delta \log G > 0.1$, however, are only observed in measurements with C8 solution and therefore very likely involve molecules. There is also an evident decrease of $\delta \log G$ with $\langle \log G \rangle$ in this case, which suggests that the fluctuations with large relative amplitude are only possible when the conductance of the junction is comparable to that of the molecules.

The large amplitudes of molecule-caused fluctuations should allow investigation of such signals despite the background caused by thermal movement. Those fluctuations are going to be the topic of the following sections.

3.2 Focus on Few-Level Oscillations

The oscillations between two or few well-defined conductance values sometimes observed in the fixed position measurements described in the previous section produced interest in their properties. The main goal of the present work was to examine those random telegraph signals (RTS), distinguish them from 1/f noise and investigate the influence of the measured molecules on the signal. Conductance oscillations with molecules have been observed before, for example in STM break junction measurements in liquid [15] (attributed to binding/unbinding of molecules) and angle evaporation nanogaps in vac-

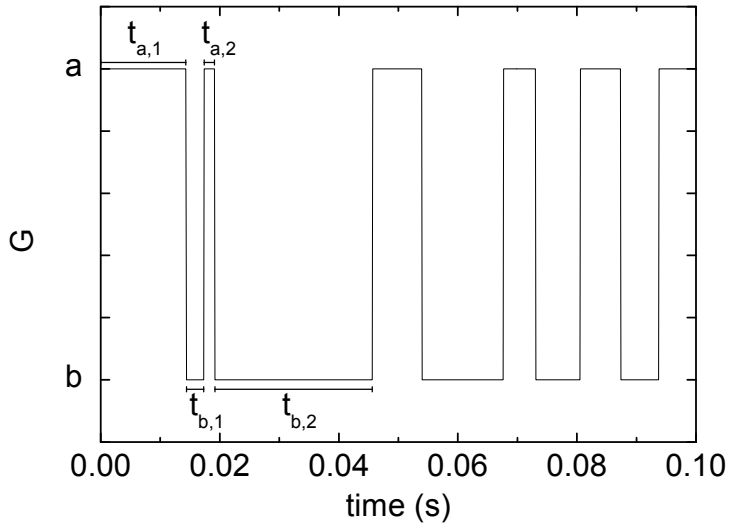

FIGURE 3.4: Theoretical two-level RTS signal with conductance values $G_{high} = a$ and $G_{low} = b$. Average lifetimes $\tau_a = \langle t_{a,i} \rangle = 10\,\text{ms}$ and $\tau_b = \langle t_{b,i} \rangle = 5\,\text{ms}$.

uum at 4 K [16] (thought to be caused by binding/unbinding of a proton to the sulfur of the molecule that binds to the gold electrode).

3.2.1 Random Telegraph Signals in Theory

A perfect RTS consists of two or more different values that the measured signal can take. We are mainly interested in the case of only two different values. Each time a value a or b is reached, the signal will stay there for a random lifetime $t_{a,i}$ or $t_{b,i}$, respectively, before switching to the other value. Those lifetimes $t_{a,i}$ and $t_{b,i}$ are exponentially distributed with average lifetimes $\tau_a = \langle t_{a,i} \rangle$ and $\tau_b = \langle t_{b,i} \rangle$. This means that there is a constant probability density for an active state to decay into the other one. Figure 3.4 shows a simulated example of a two-level RTS.

Random telegraph signals (RTS) were first observed in semiconductor devices (usually called random telegraph noise or burst noise). The most common cause of RTS in semiconductors is the trapping and release of charge carriers which affects the conductance. RTS is also observed in metallic point contacts where thermal and current-induced atomic rearrangement leads to changes of the conductance [17]. In our measurements of break junctions in liquid, RTS could be caused by atomic rearrangements of the electrode tips (change in tunneling distance or molecule–metal bond conformation), binding and unbinding of molecules from an electrode or structural or electronic changes within molecules.

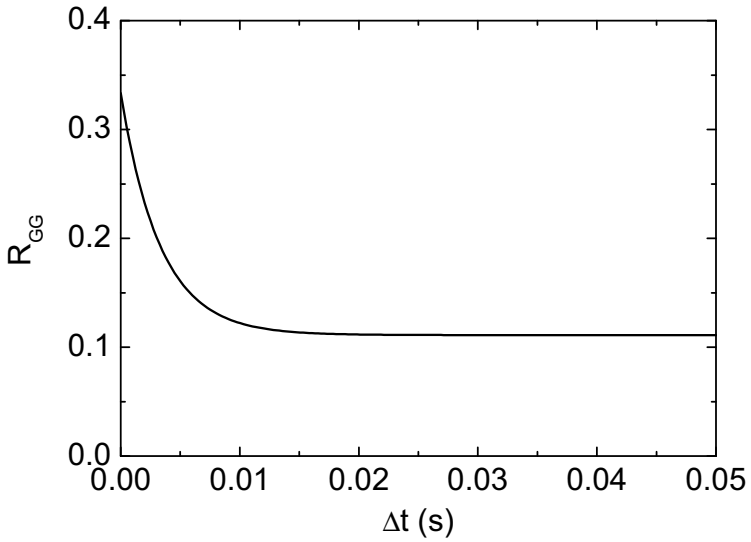

FIGURE 3.5: Theoretical autocorrelation of a RTS with $\tau_a = 10\,\text{ms}$, $\tau_b = 5\,\text{ms}$, $a = 1$ and $b = 0$.

3.2.2 Methods to Analyze Random Telegraph Signals

Several methods can be utilized to analyze random telegraph signals or check for their occurrence in recorded conductance traces. In this work, the auto correlation, the power spectrum and lifetime histograms have been calculated of measured data and used for these purposes. In this section we discuss each method and show theoretical results for a two-level RTS with $\tau_a = 10\,\text{ms}$ and $\tau_b = 5\,\text{ms}$ as illustrated in figure 3.4.

The autocorrelation function ($R_{xx}(\Delta t) = \lim_{T\to\infty} \frac{1}{T} \int_0^T x(t) \cdot x(t + \Delta t)\, dt$) of a perfect two-level RTS $G(t)$ is given by the exponential decay shown in equation 3.2 with the second term being zero when the average value $\langle G \rangle$ is first subtracted from the signal (a derivation can be found in appendix A.2).

$$R_{GG}(\Delta t) = \frac{\tau_a \tau_b (a-b)^2}{(\tau_a + \tau_b)^2} e^{-\Delta t\left(\tau_a^{-1} + \tau_b^{-1}\right)} + \left(\frac{\tau_a a + \tau_b b}{\tau_a + \tau_b}\right)^2 \tag{3.2}$$

Figure 3.5 shows the theoretical autocorrelation for an RTS. Using equation 3.2 we are able to extract the relaxation time $\tau = \left(\tau_a^{-1} + \tau_b^{-1}\right)^{-1}$ from an exponential decay fit to the autocorrelation of a measured trace. Disadvantages of this method include the inability to separately obtain τ_a and τ_b and the influence of other components of the signal apart from RTS on the results.

The Fourier transform of the autocorrelation function (power spectrum) is given by equation 3.3 with $w_a = \frac{\tau_a}{\tau_a + \tau_b}$ and $w_b = \frac{\tau_b}{\tau_a + \tau_b}$ the probabilities of the two states and the relaxation time τ. The $-3\,\text{dB}$ frequency of the Lorentzian spectrum (where the power density is half the value for $f = 0$) is $f_{-3\,dB} = \frac{1}{2\pi\tau}$.

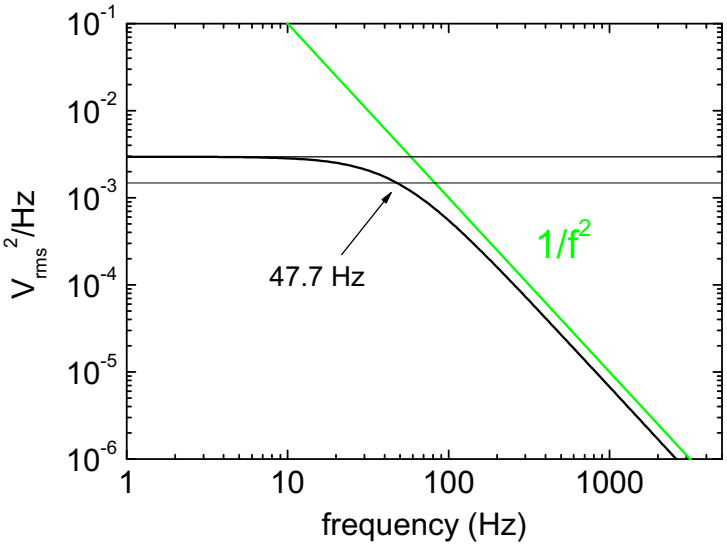

FIGURE 3.6: Theoretical power spectrum of a RTS with $\tau_a = 10\,\text{ms}$, $\tau_b = 5\,\text{ms}$, $a = 1$ and $b = 0$. $-3\,\text{dB}$ frequency $f_{-3\,dB} = 47.7\,\text{Hz}$.

$$S_G(f) = \frac{4w_a w_b \left(a-b\right)^2 \tau}{1 + 4\pi^2 f^2 \tau^2} \tag{3.3}$$

As seen in equation 3.3 and figure 3.6, a power spectrum of clear RTS is flat at low frequencies and decays proportionally to $1/f^2$ for $f \gg f_{-3\,dB}$. With both axes plotted logarithmically this translates to a slope of 0 and -2 for low and high frequencies, respectively. Calculating the slopes of such logarithmic spectra seems therefore a viable technique to differentiate RTS from $1/f$ noise or white noise. It should be noted, however, that a sum of many Lorentzian spectra with their $-3\,\text{dB}$ frequencies distributed like $D\left(f_{-3\,dB}\right) = 1/f_{-3\,dB}$ results in a $1/f$ spectrum.

The final method used was to calculate lifetime histograms. For a perfect two-level RTS, we expect the lifetime distributions of both conductance states to be exponential decays with the average lifetime $\tau_{state} = \tau_a$ or τ_b. The counts in a lifetime histogram of one state are given by equation 3.4 (ΔT the measurement/RTS duration (whichever is shorter), Δt the histogram bin size, A the total prefactor of the exponential).

$$N_{hist}\left(t\right) = \frac{\Delta T \Delta t}{\left(\tau_a + \tau_b\right) \cdot \tau_{state}} \cdot \exp\left(-\frac{t}{\tau_{state}}\right) = A \cdot \exp\left(-\frac{t}{\tau_{state}}\right) \tag{3.4}$$

The total number of switching events from one state during one measurement is given by $N_{tot} = \frac{\Delta T}{(\tau_a+\tau_b)} = A\frac{\tau_{state}}{\Delta t}$ (for $N_{tot} \gg 1$). If a measured signal shows clear two-level RTS, we expect exponential decays in the lifetime histograms with the two decay constants corresponding directly to the average lifetimes of the two states. Only for very

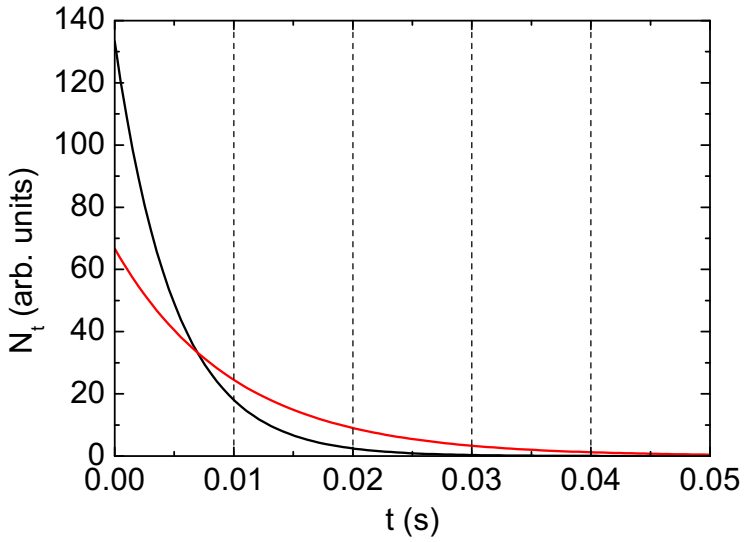

FIGURE 3.7: Theoretical lifetime histograms of a RTS with $\tau_a = 10\,\text{ms}$, $\tau_b = 5\,\text{ms}$. The histograms of $t_{a,i}$ and $t_{b,i}$ are shown in red and black, respectively.

low t values there could be deviations caused by the limited frequency bandwidth or sampling rate.

If the signal consists of phases with two different average lifetimes for one conductance state, we expect the lifetime histogram to be described by a sum of two exponential functions with their weights $W = A\tau_{state}$ being proportional to the number of switching events per phase. The lifetime histogram method allows to directly obtain the average lifetimes of both states which is a big advantage over the other methods. A disadvantage is that the individual lifetimes of the states have to be known first.

In the following sections, we will present measured RTS and apply the described analyzation methods.

3.2.3 Measured Random Telegraph Signals

As the probability of observing stable RTS with automated nonselective measurements is quite low, they were actively sought after. The junction was cycled a few times to relax the electrodes and then slowly closed from a conductance below the detection limit of around $3 \cdot 10^{-7}\,G_0$ (depending on the solvent). The motor was stopped from time to time to subjectively screen the conductance trace for RTS while it was sampled at 50 Hz and displayed live on the computer screen. When an interesting signal was observed, a recording at higher sampling rate was started with the gain fixed (typically 100 traces of 1 second with a sampling rate of 10 kHz).

Measurements in pure mesitylene mainly show 1/f noise with very few jumps between discrete values and no large amplitude oscillations (see figure 3.8 for a typical mesitylene

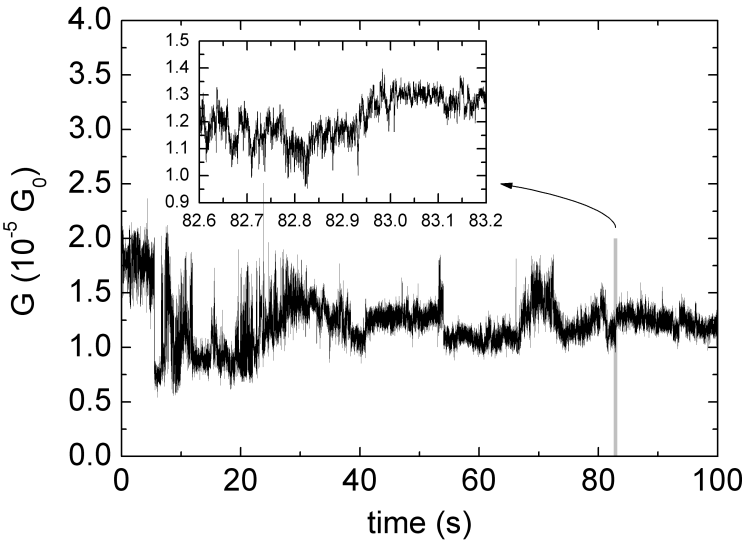

FIGURE 3.8: Typical conductance trace with mesitylene. Mainly random fluctuations are visible without any two-level oscillations.

measurement). Low-amplitude oscillations were observed only once in mesitylene, lasting for about 8 seconds. With alkanedithiols, on the other hand, RTS signals were observed more often (in the order of twice per hour). The oscillations lasted for several seconds, sometimes exceeding the recording time of 100 seconds. Figures 3.9, 3.10 and 3.11 show recordings of clear RTS in C6 and C9 solutions. Measurements with S-OPE-S showed less stable oscillations (figure 3.12 shows an example with three-level RTS). With N-OPE-N it was even more rare to witness RTS and it typically lasted for a few seconds only. Figure 3.13 shows an example.

In some measurements, the observed RTS had lifetimes close to or below the minimum observable time interval of 1 ms or 0.2 ms defined by bandwidth and sampling rate (depending on the gain setting). It might therefore be useful to try to get a larger measurement bandwidth for further measurements.

These measurements and others are going to be analyzed in the following sections.

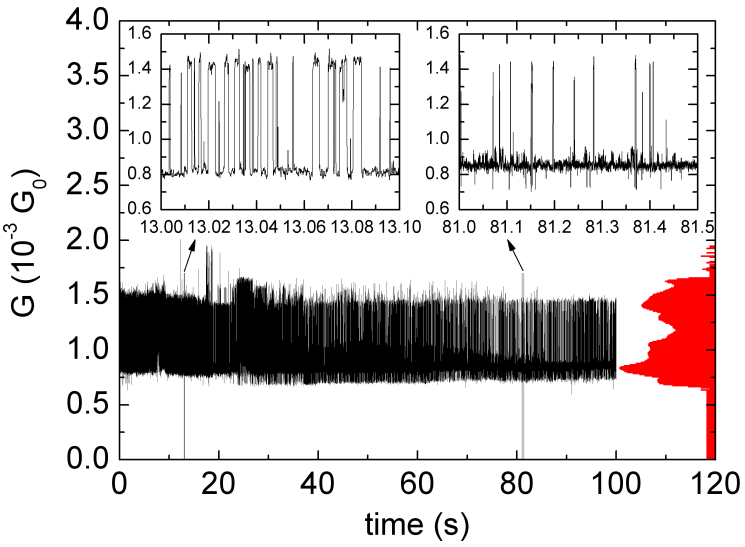

FIGURE 3.9: Conductance trace with C6 showing clear and stable RTS that is first strictly two-level but also shows two additional levels with little statistical weight slightly above and below the main low level after $\approx 25\,\mathrm{s}$ (see the red histogram with logarithmic counts scale).

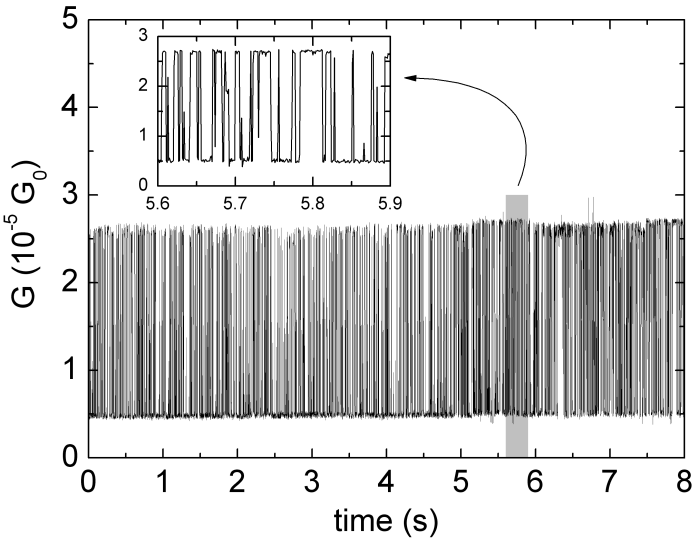

FIGURE 3.10: Conductance trace with C9 showing clear and stable two-level RTS.

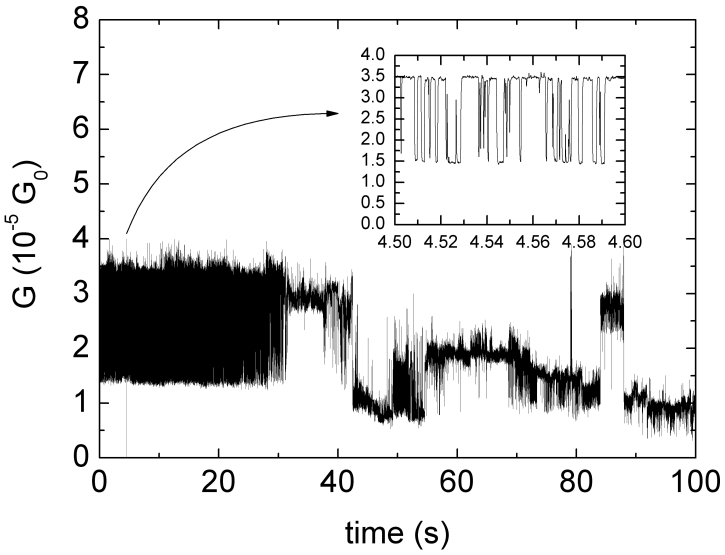

FIGURE 3.11: Conductance trace with C9 showing RTS during the first $\approx 30\,\mathrm{s}$. There appear to be phases with at least two different lifetimes for both the high and low conductance states. This is also supported by the lifetime histogram in figure 3.19.

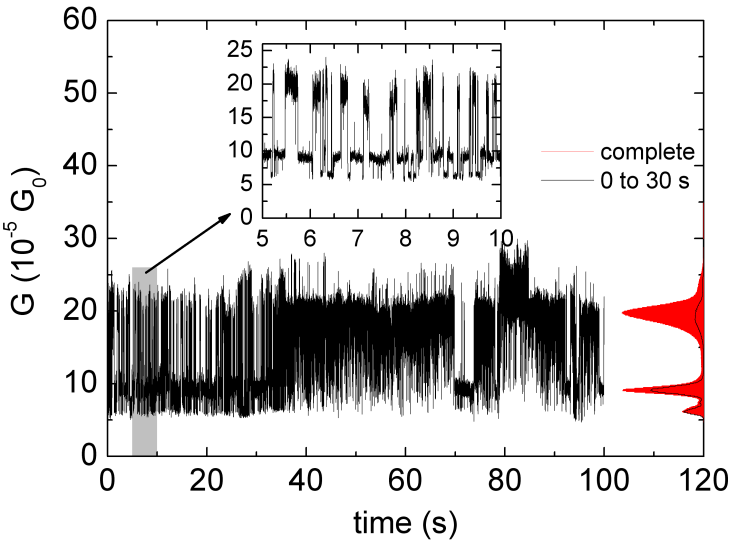

FIGURE 3.12: Conductance trace with OPE. Conductance histograms of the complete measurement (red) and the first 30 seconds are shown on the right.

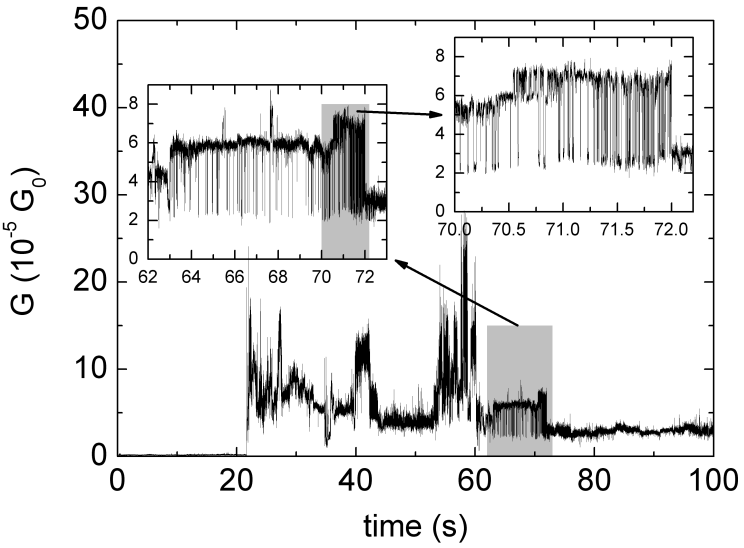

FIGURE 3.13: Conductance trace with N-OPE-N. About 10 s of RTS are found in the otherwise irregular signal.

3.2.4 Autocorrelation

The autocorrelation of several measured conductance traces has been calculated. Two examples are shown here. The autocorrelation of the C9 signal shown in figure 3.11 does agree with an exponential decay during the first few ms (figure 3.14), with the fit leading to a relaxation time of $\tau = 0.55\,\mathrm{ms}$.

There are other cases where a single exponential is not sufficient. Figure 3.15 (C6) shows such an example where the autocorrelation does not fit a single exponential well but has a slowly decaying component as well (lifetime about 20 times higher). Such a slowly decaying component is also visible in figure 3.14 but as the main component is decaying faster here, it has little influence on the fit.

The autocorrelation can be used for a rough estimate of the relaxation time but its exact shape is influenced by many features of the signal. It would therefore be difficult to use it to automatically identify RTS.

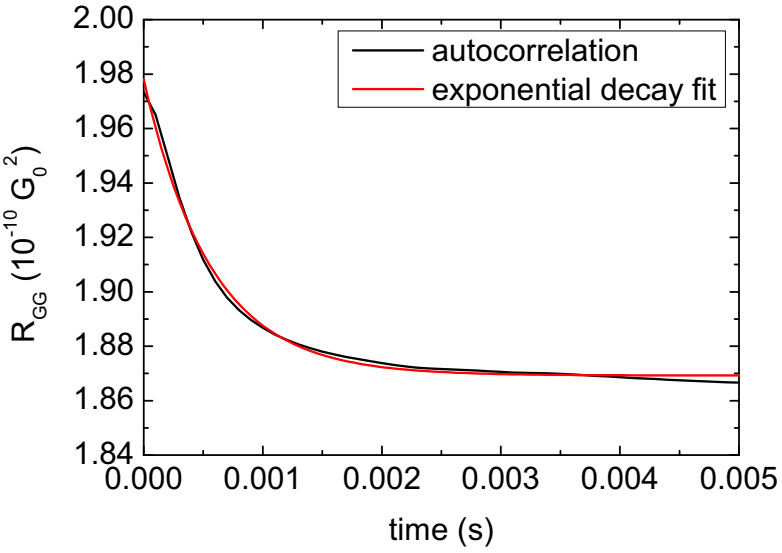

FIGURE 3.14: The autocorrelation (black) of the signal measured with C9, shown in figure 3.11. The exponential decay fit (red) leads to a relaxation time of $\tau = 0.55 \pm 0.01$ ms.

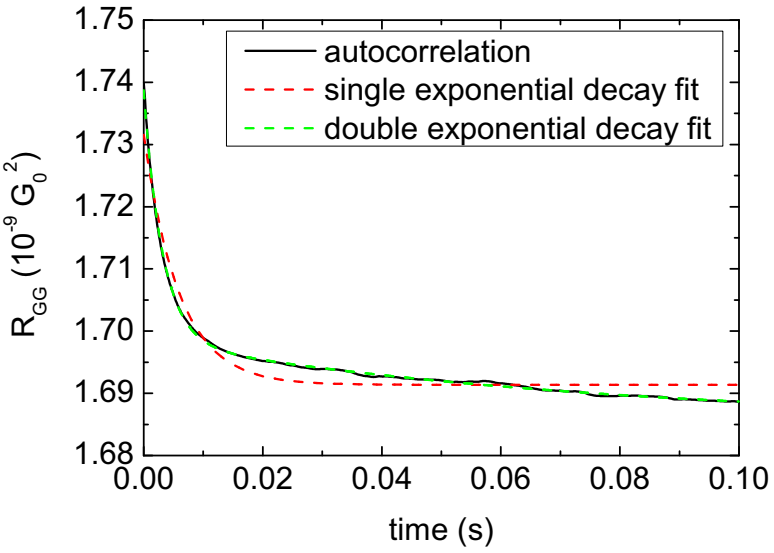

FIGURE 3.15: Autocorrelation function of a measurement with C6. The single exponential does not fit nicely and leads to $\tau = 5.96 \pm 0.11$ ms whereas the double exponential fit is quite convincing, resulting in $\tau_{fast} = 3.16 \pm 0.01$ ms and $\tau_{slow} = 74.8 \pm 2.0$ ms.

3.2.5 Power Spectrum

In the experiment, the spectra were calculated from the recorded 1 second intervals by a LabVIEW VI, leading to a frequency range of 1 to 5000 Hz. Several consecutive 1 second spectra of the time interval of interest were averaged. As predicted in section 3.2.2, the spectrum of a well-defined RTS like the C9 one shown in figure 3.11 is a Lorentzian (figure 3.16, black). The later part of the measurement without RTS results in $1/f$ noise (red). There are downward kinks in the spectra at a frequency of about 1000 Hz leading to a slope steeper than $1/f^2$ or $1/f$ for high frequencies which are caused by the upper frequency limit of the setup (for bandwidth measurements see appendix B.3). We notice in figure 3.16 that the RTS spectrum is not completely flat at low frequencies. This is caused by a small amount of $1/f$ noise also present in the signal. In other measurements, this $1/f$ component of the signal is even more pronounced. The fact that the spectrum is not flat at low frequencies makes it difficult to accurately estimate the -3 dB frequency of a spectrum and thereby the relaxation time τ of the RTS. In the example shown, the -3 dB frequency is about 200 Hz which corresponds to $\tau \approx 0.8$ ms.

The slopes of the spectra seem to be a possible criterion to identify RTS as a distinct difference between RTS and non-RTS signals is expected. To investigate this idea, the slopes of several spectra were calculated between 200 and 800 Hz. Looking at the scatter plot (figure 3.17), we see the slopes varying from -1.0 to -1.8 with some flatter outliers which are a result of strong white background noise in comparison to the signal (at low conductance) or short relaxation time of the RTS signal which leads to an expected -3 dB point of the RTS spectrum above the frequency limit of the IV converter. There is no clear separation between measurements showing 1/f noise and measurements showing RTS. Instead, there seems to be a continuous distribution of possible slope values even for signals showing RTS (filled symbols). A slightly more reliable way might be to calculate differences between slopes at low and high frequencies as plotted in figure 3.18. Here, any background noise with a constant slope (e.g. $1/f$ noise) is canceled out. Still, it is not easy to clearly differentiate RTS from $1/f$ noise with this method.

In conclusion, calculating the slope at two fixed frequency intervals does not seem to be a reliable way to identify RTS in our setup. Calculating a list of slopes at many different frequency intervals and comparing the maximum and minimum might be a more reliable method but has not been done in this work.

3.2.6 Distribution of Lifetimes

The lifetimes of the high ($t_{a,i}$) and low ($t_{b,i}$) conductance states were obtained by analyzing the conductance signal with a LabVIEW VI in the following way. Three reference levels low, mid and high are defined to be usually 10, 50 and 90 %, of the range between low and high conductance states. The time interval between one mid reference level crossing and the closest following one that occurs after at least one crossing of a high or low reference level then corresponds to a high- or low-state lifetime. This method only works if the RTS amplitude is larger than the background noise.

Histograms of such obtained lifetimes from a C9 measurement are shown in figure

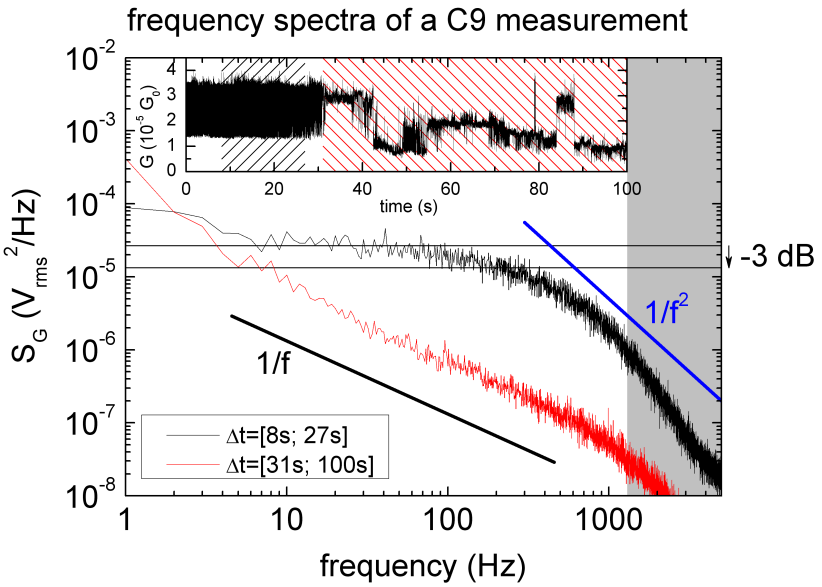

FIGURE 3.16: Spectra of the C9 measurement shown in figure 3.11. The black spectrum is calculated from the period with stable RTS observed in the beginning (inset, shaded in black) which translates into a Lorentzian spectrum. The signal did not show regular features later (31 to 100 seconds) which leads to a 1/f spectrum (red). The RTS spectrum has a -3 dB point of about 200 Hz which means that $\tau \approx 0.8$ ms. The $1/f$ and $1/f^2$ lines are included as guides to the eye. The gray area indicates frequencies higher than the bandwidth of the setup.

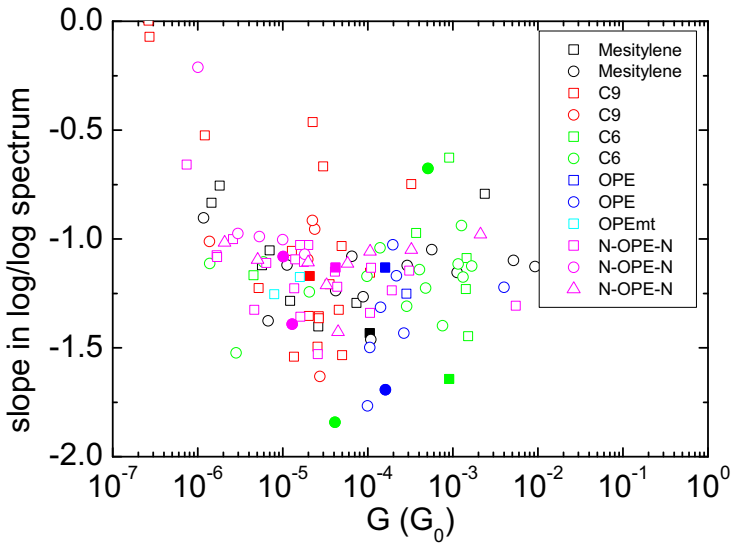

FIGURE 3.17: Fitted slopes of several spectra both with and without clear RTS. The filled symbols indicate those measurements with RTS, that were investigated in the following sections. The fit region was from 200 to 800 Hz.

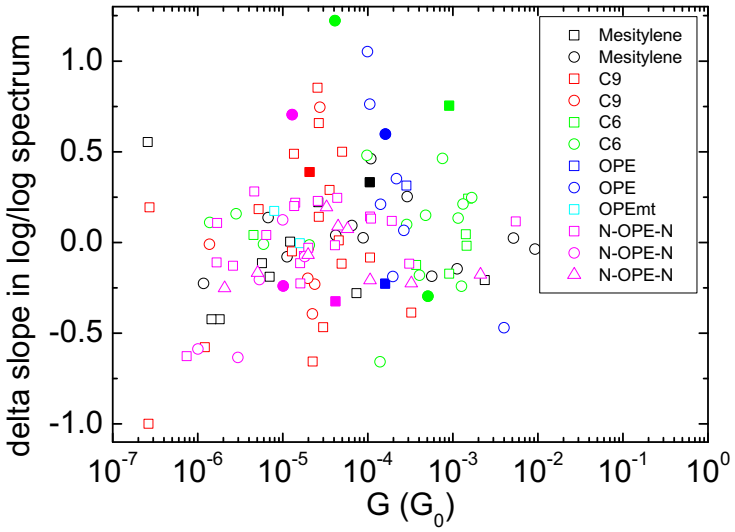

FIGURE 3.18: The slopes at low frequency (1 to 60 or 1 to 500 Hz) minus the slopes at high frequency (200 to 800 Hz).

3.19. They show smooth decay as predicted in section 3.2.2 (no obvious features at 20 or 10 ms that could have been caused by 50 Hz line noise). For this measurement, single exponential functions do not allow for an accurate fit but sums of two exponentials do. This suggests that there were at least two distributions of lifetimes for both conductance states with different average lifetimes in the analyzed signal. The single exponential fits lead to average lifetimes $\tau_a = 1.92\,\text{ms}$ (high conductance state) and $\tau_b = 0.93\,\text{ms}$ (low conductance state) which results in a relaxation time of $\tau = 0.63\,\text{ms}$, approximately agreeing with the values obtained from the spectrum and the autocorrelation. Fitting the sum of two exponentials results in good fits with $\tau_{a,slow} = 3.6\,\text{ms}$ and $\tau_{b,slow} = 2.0\,\text{ms}$ (relaxation time $\tau_{slow} = 1.3\,\text{ms}$) with most of the weights $A\tau$ and $\tau_{a,fast} = 0.53\,\text{ms}$ and $\tau_{b,fast} = 0.41\,\text{ms}$ (relaxation time $\tau_{fast} = 0.23\,\text{ms}$) with 30 % and 47 % of the total number of switching events, respectively.

In some measurements with RTS, the lifetime histograms show exponential decay that is nearly perfectly described by a single exponential function. Figure 3.20 shows such an example with C6. From the clear exponential distribution of the lifetimes of both states, we conclude that the decay constants of the two states stay the same during the observed RTS (duration 59 s) which suggests that the activation energies necessary for jumping from one state to the other are not changing.

As very clean single exponential decays are rare, the average lifetimes τ_a and τ_b were calculated for several measurements showing RTS by fitting the sum of two exponentials to lifetime histograms and choosing the lifetime value with the most weight $A\tau_{state}$. Figure 3.21 shows the obtained values for several measurements with mesitylene, alkanedithiols (C5, C6, C9), octanemonothiol (C8mt) and OPE dithiol (OPE) as well as

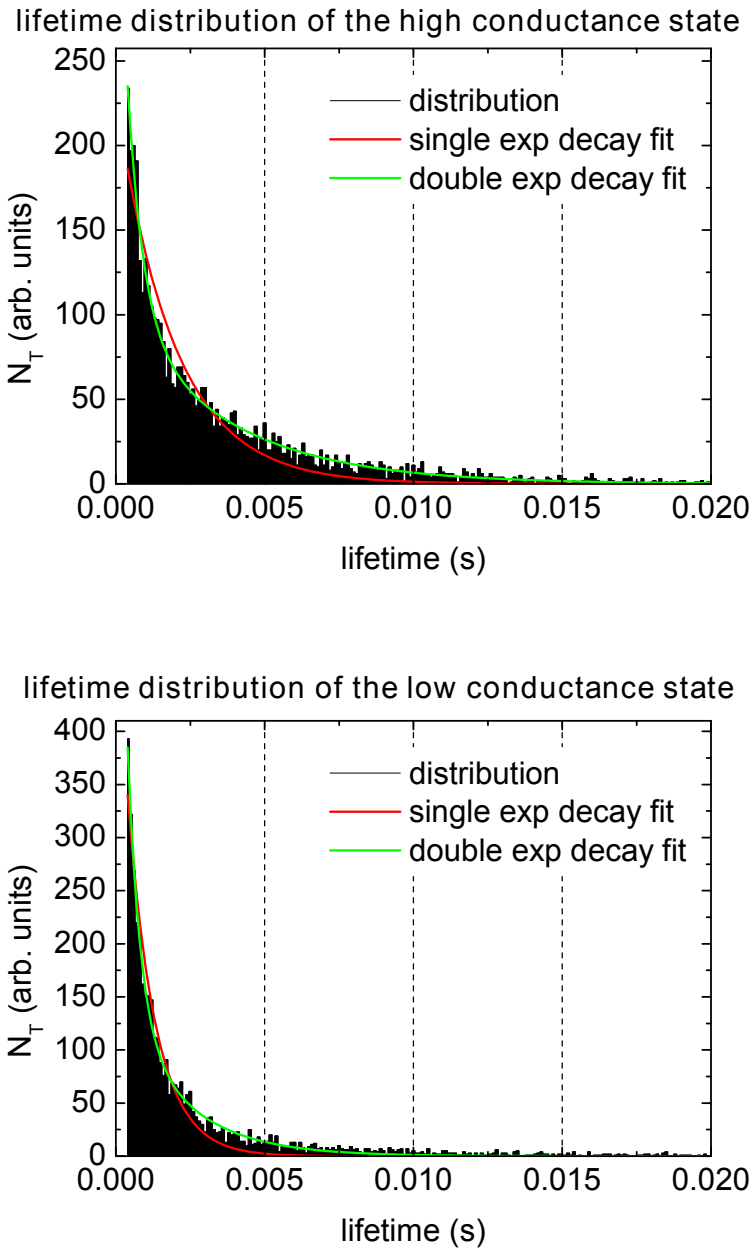

FIGURE 3.19: Histograms of the lifetimes of the high (top) and low (bottom) states of the C9 measurement shown in figure 3.11. Single exponential functions don't fit the histograms well but the sum of two exponentials does which means that in part of the analyzed signal the lifetimes were different.

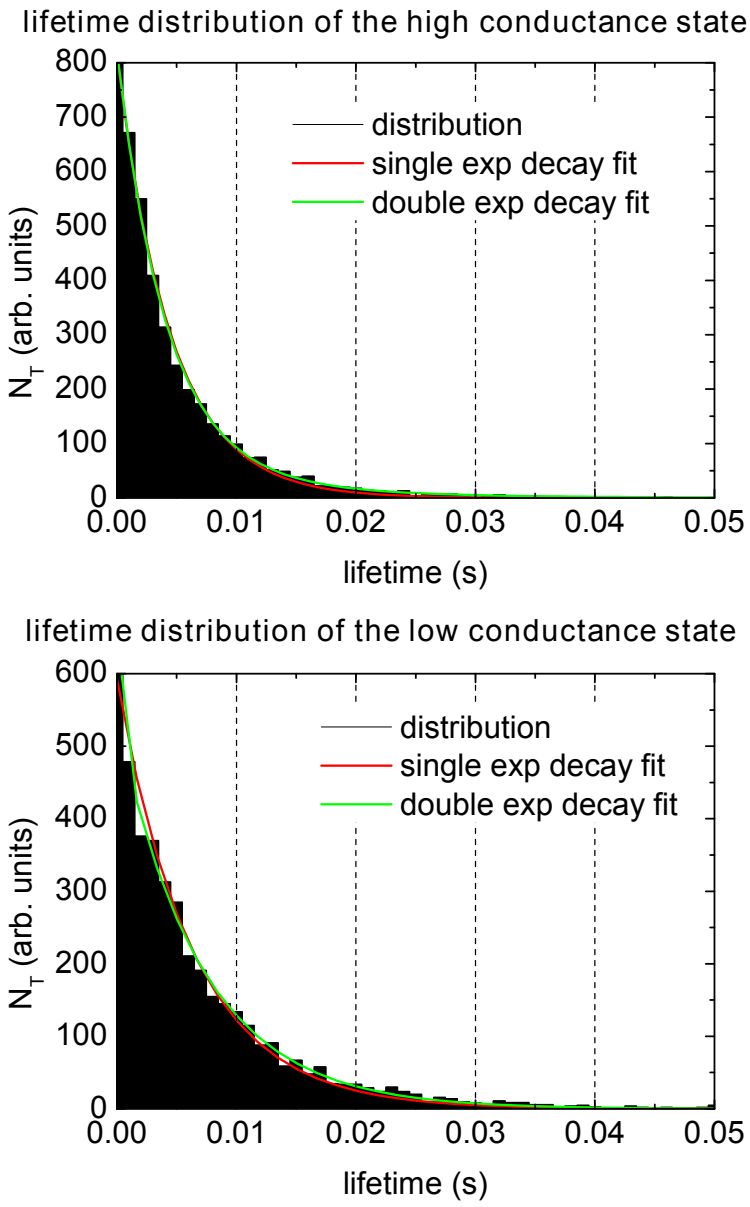

FIGURE 3.20: Histograms of the lifetimes of the high (top) and low (bottom) conductance states of a C6 measurement. Single exponential functions fit the data well with little improvement from adding a second exponential. $\tau_a = 4.52\,\text{ms}$ and $\tau_b = 6.32\,\text{ms}$ (relaxation time $\tau = 2.64\,\text{ms}$, approximately agreeing with τ_{fast} obtained from the autocorrelation fit in figure 3.15).

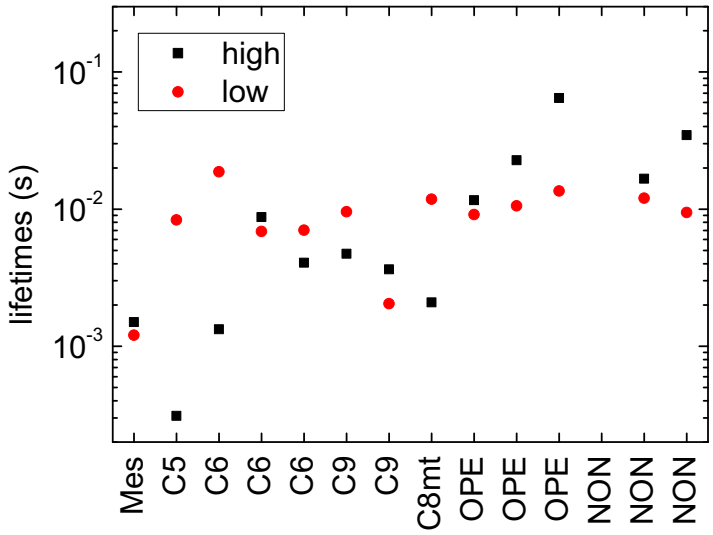

FIGURE 3.21: Average lifetimes τ_a (black) and τ_b (red) from several measured RTS with pure mesitylene, alkanedithiols (C5, C6, C9), octanemonothiol (C8mt) and OPE dithiol (OPE) as well as OPE dipyridine (NON).

OPE dipyridine (NON). In average, the lifetimes are shorter for alkanedithiols than for OPE molecules. Also, the low conductance state is the more stable one for 4 out of 6 alkanedithiol measurements whereas the high conductance state is more stable for all 5 OPE measurements showing RTS.

3.2.7 Amplitude of the Random Telegraph Signals

The high (G_a) and low (G_b) conductance values of measured RTS were obtained by averaging over time intervals during which no switching to the other state occurred. The observed relative amplitudes $\Delta G_{rel} = (G_a - G_b)/G_b$ of the RTS varied a lot between measurements, taking values from close to zero up to around 5. Figure 3.22 shows the ΔG_{rel} values for the same measurements investigated above. The high values are thought to be caused by jumps between zero and one molecule bridging the gap and are observed rarely. Values around 1 might correspond to a second molecular junction being formed in addition to an existing one. Finally, the very low amplitudes are attributed to rearrangements in the gold electrodes. Because of the limited number of observed RTS and the broad distribution of amplitudes in this work, this assignment is not certain. When we compare G_{low} and G_{high} to the range of conductance observed in contact mode cycle measurements of the same molecules (horizontal bars in figure 3.23), we notice that in both cases with large amplitudes ($\Delta G_{rel} \approx 5$), G_{low} is below the range of conductance for the particular molecules. This supports the assumption that we observe oscillations between zero and one molecule in these cases.

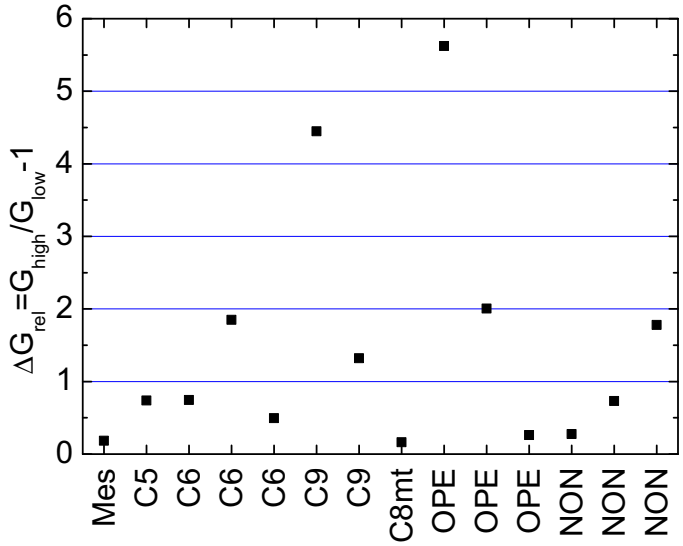

FIGURE 3.22: The relative amplitudes of observed RTS. We observe that the amplitude is either much lower than G_{low} ($\Delta G_{rel} \approx 0.2$), about the same ($\Delta G_{rel} \approx 1$), about twice the value ($\Delta G_{rel} \approx 2$) or (more rarely) much higher ($\Delta G_{rel} \approx 5$).

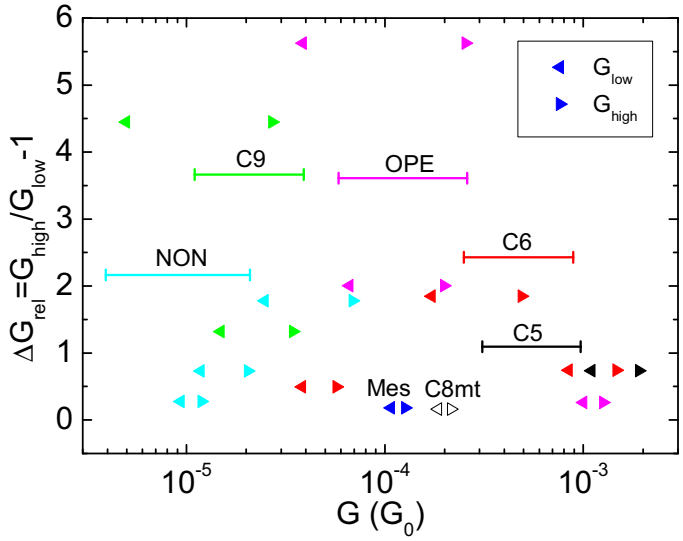

FIGURE 3.23: The relative amplitudes shown in figure 3.22 in relationship to G_{low} (◁) and G_{high} (▷). The horizontal bars represent the range of conductance values observed in contact mode cycle measurements (68 % confidence intervals).

3.2.8 Noise Levels on The two Conductance Levels

The background noise levels on the two conductance states of measured RTS were investigated. For each measurement, the average conductance values G_a and G_b and the standard deviations δG_a and δG_b were calculated from equally long time intervals of the high and low conductance states. All values are plotted in figure 3.24. It can be seen that for almost all measurements, the noise is stronger during the high conductance state (one C5 measurement being the exception). Also, the difference in noise seems more pronounced for S-OPE-S than for the other investigated molecules.

One known cause for different measured noise levels on RTS states are different average lifetimes that lead to different observable bandwidths by defining a low-frequency limit. If the background noise is assumed to be white and of constant power, the observed intensity is proportional to the bandwidth. An even larger effect would be expected with $1/f^{\alpha}$ background noise [18].

Assuming constant white background noise, the expected ratio $\delta G_a/\delta G_b$ has been calculated according to equation 3.5 for the lower frequency bounds $f_{min,a} = \tau_a^{-1}$ and $f_{min,b} = \tau_b^{-1}$ and upper frequency limits f_{max} of 1.3 kHz or 10 kHz for the gain settings 10^9 or $0.22 \cdot 10^8\, V/A$, respectively. Figure 3.25 shows the measured ratios between noise levels on high and low conductance states (black) and also the expected ratios calculated from the lifetimes and bandwidth (red).

$$\delta G_a/\delta G_b = \sqrt{\frac{f_{max} - \tau_a^{-1}}{f_{max} - \tau_b^{-1}}} \tag{3.5}$$

This effect explains the ratio of noise amplitudes observed in the C5 measurement: The average lifetimes were very different with $\tau_a = 0.31\,\text{ms}$ and $\tau_b = 8.34\,\text{ms}$. These result in lower frequency bounds of $f_{min,a} = \tau_a^{-1} = 3200\,\text{Hz}$ and $f_{min,b} = \tau_b^{-1} = 120\,\text{Hz}$. Together with the upper frequency limit of the measurement ($f_{max} \approx 10\,\text{kHz}$), the different observable bandwidths alone account for a substantial difference of the observed noise if the background noise is assumed to be constant and white.

For most measurements, though, the differences between the lifetimes are not large enough to account for the observed differences between background noise levels and would even lead to disagreeing expected and measured orders of the expected noise levels in some cases. This means that the assumption of constant white background noise is not fulfilled. Also, the difference in observable bandwidth seems to be negligible for most measurements.

To see directly how strongly the background noise levels on the conductance states vary with their average conductance, the coefficient $\Delta\delta G/\Delta\langle G\rangle = (\delta G_a - \delta G_b)\,/\,(G_a - G_b)$ was calculated. In figure 3.26 we see that the dependence is much stronger on average for both OPE dithiol and OPE dipyridine than for the alkanedithiols.

3.2.9 Limitations of The Used Methods

The methods used in sections 3.2.6 to 3.2.8 cannot be used unless the amplitude of the RTS is sufficiently larger than the background noise. There are more complex methods

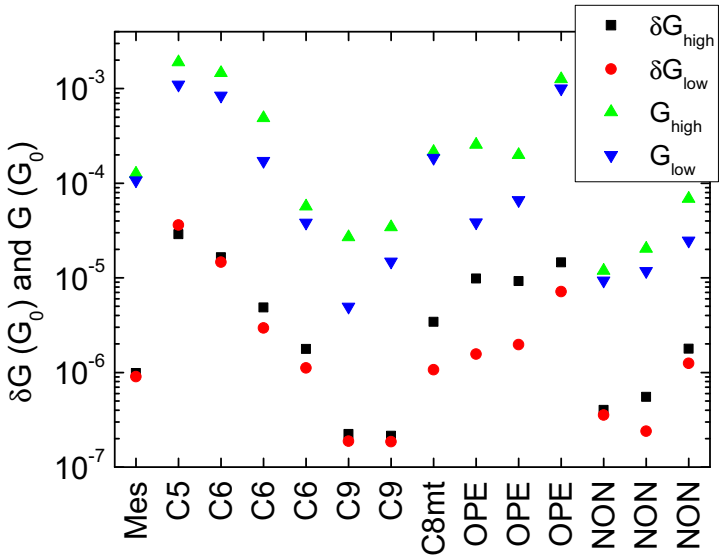

FIGURE 3.24: Standard deviations and averages of the conductance values over equally long time intervals of both high and low conductance states for each measurement.

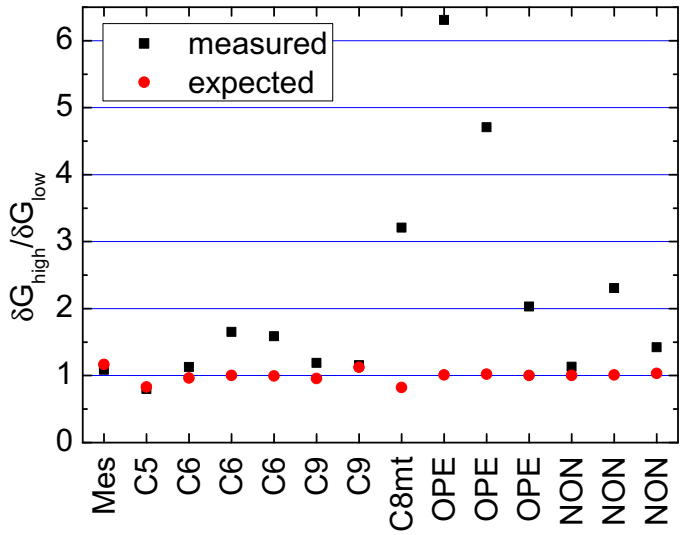

FIGURE 3.25: The ratio between the standard deviations of the signal on the high and low conductance states of measurements showing RTS (black). A theoretical ratio was estimated from the average lifetimes of the two conductance states by assuming constant white background noise (red). In general, the two values do not agree.

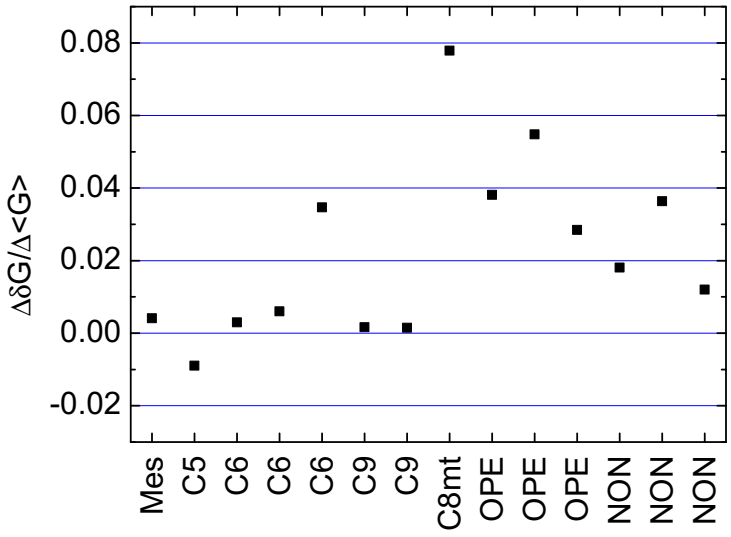

FIGURE 3.26: The dependence of the background noise levels on the conductance.

for investigating RTS that might prove useful for some analysis. For example, the average conductance values of each state and their relative average lifetimes can be obtained by fitting a sum of Gaussian distributions to the conductance histogram of the recorded data. The absolute average lifetimes can then be obtained in an iterative procedure that assigns each data point to one conductance state and allows separation of the signal into RTS and background noise. This method could in principle also be used for more than two conductance states [19]. An alternative method that does not depend on predetermined values for the states is to detects the jumps with different threshold values and then choosing the best threshold value by comparing the noise power in the signal after subtracting the RTS signal [20].

3.3 Results

Random telegraph signals have been observed with solutions of alkanedithiols and OPE dithiols and dipyridines. Overall, RTS was observed more often with alkanedithiols (in the order of twice per hour) than with OPEs (no observed RTS for several samples). The state lifetimes appear to be longer for both OPE variants than for the alkanedithiols. Thereby, the low-conductance state lifetime τ_b is similar for both groups of molecules but τ_a is longer for the OPEs. This can be interpreted to mean that it takes a similar amounts of time to form new metal–molecule bonds for both groups but that the bonds are more stable for the OPEs. The longer bond lifetime might be due to π–π interactions between the OPE molecules. Also, the background noise amplitude on the RTS states seems to depend strongly on the conductance for S-OPE-S and N-OPE-N but not for the alkanes.

4 Conclusion and Outlook

In this work, MCBJs have been used to measure the conductance of metal–molecule–metal junctions for different molecules. The previously reported exponential dependence of the conductance on the length of the molecules has been confirmed for alkanedithiols. Conductance traces recorded during fixed position intervals in-between small closing steps show fluctuations $\delta \log G$ that are small and approximately independent of $\langle G \rangle$ with pure mesitylene. In contrast, they are of larger amplitude and clearly depending on $\langle G \rangle$ for C8 solution, suggesting an involvement of the molecules. Large-amplitude RTS that were found in some of the C8 fixed position measurements motivated a manual search for more of those signals. RTSs were observed more often with alkanedithiols than with OPEs but still relatively rarely. The lifetime of the low conductance state (τ_b) was found to be similar for both groups of molecules whereas the lifetime of the high conductance state (τ_a) is longer for the OPEs. RTS traces for OPEs show considerably more background noise on the high conductance state than on the low state (S-OPE-S more so than N-OPE-N) whereas there is only a small difference in background noise for the alkane dithiols. This suggests that metal–OPE–metal junctions are inherently noisier than metal–alkane–metal junctions and gaps without molecules which might be due to the rigidity (less accommodation of gold movement) and higher conductance of the OPE backbone.

It should be mentioned that the number of observed RTS in this work was quite low and an influence of manual data selection or statistical coincidence cannot definitely be ruled out. For a more thorough investigation of the subject, an automated measurement system with RTS detection might be well-advised in order to get more data more objectively. A disadvantage of the fixed position technique in contrast to dynamic techniques is that the forces between the electrodes and the molecules are unknown variables. Measurements with a conductive AFM could allow at least the total force to be known.

Regarding future applications of molecular electronics, fundamental research of molecule–metal contacts is definitely important. A long lifetime and a defined coupling constant are both required for most imaginable applications. From our measurements, it seems that a single chemical bond is not stable enough for long-lived devices. Dendrimeric molecules with many linker groups could allow lifetimes long enough for practical use. As the mobility of the surface atoms of gold might be a cause of the short bond lifetimes, another way to obtain more stable molecular junctions might be to use a less mobile material like platinum, palladium or silicon.

5 Acknowledgments

I thank Teresa González, Songmei Wu and Roman Huber for their support in the lab, Michel Calame for his help during data analysis and writing and professor Christian Schönenberger for allowing me to do this master work in his group.

Bibliography

[1] Tsutsui, M., Shoji, K., Taniguchi, M. & Kawai, T. Formation and self-breaking mechanism of stable atom-sized junctions. *Nano Letters* **8**, 345–349 (2008).

[2] González, M. T. *et al.* Electrical conductance of molecular junctions by a robust statistical analysis. *Nano Letters* **6**, 2238–2242 (2006).

[3] Akkerman, H. B. & de Boer, B. Electrical conduction through single molecules and self-assembled monolayers. *Journal Of Physics-Condensed Matter* **20**, 013001 (2008).

[4] Huber, R. *et al.* Electrical conductance of conjugated oligorners at the single molecule level. *Journal Of The American Chemical Society* **130**, 1080–1084 (2008).

[5] Huisman, E. H. *et al.* Stabilizing single atom contacts by molecular bridge formation. *Nano Letters* **8**, 3381–3385 (2008).

[6] Casparis, L., Jurcevic, P. & Schmid, S. Gold breakjunctions (2008). Blockkurs.

[7] Venkataraman, L. *et al.* Single-molecule circuits with well-defined molecular conductance. *Nano Letters* **6**, 458–462 (2006).

[8] Hybertsen, M. S. *et al.* Amine-linked single-molecule circuits: systematic trends across molecular families. *Journal Of Physics-Condensed Matter* **20**, 374115 (2008).

[9] Kiguchi, M., Miura, S., Hara, K., Sawamura, M. & Murakoshi, K. Conductance of a single molecule anchored by an isocyanide substituent to gold electrodes. *Applied Physics Letters* **89**, 213104 (2006).

[10] González, M. T. *et al.* Conductance values of alkanedithiol molecular junctions. *New Journal Of Physics* **10**, 065018 (2008).

[11] Xu, B. Q. & Tao, N. J. J. Measurement of single-molecule resistance by repeated formation of molecular junctions. *Science* **301**, 1221–1223 (2003).

[12] Li, C. *et al.* Charge transport in single au vertical bar alkanedithiol vertical bar au junctions: Coordination geometries and conformational degrees of freedom. *Journal Of The American Chemical Society* **130**, 318–326 (2008).

[13] Wu, S. M. *et al.* Molecular junctions based on aromatic coupling. *Nature Nanotechnology* **3**, 569–574 (2008).

[14] Grüter, L., González, M. T., Huber, R., Calame, M. & Schönenberger, C. Electrical conductance of atomic contacts in liquid environments. *Small* **1**, 1067–1070 (2005).

[15] Huang, Z. F., Chen, F., Bennett, P. A. & Tao, N. J. Single molecule junctions formed via au-thiol contact: Stability and breakdown mechanism. *Journal Of The American Chemical Society* **129**, 13225–13231 (2007).

[16] Danilov, A. V., Kubatkin, S. E., Kafanov, S. G., Flensberg, K. & Bjørnholm, T. Electron transfer dynamics of bistable single-molecule junctions. *Nano Letters* **6**, 2184–2190 (2006).

[17] Agraït, N., Yeyati, A. L. & van Ruitenbeek, J. M. Quantum properties of atomic-sized conductors. *Physics Reports-Review Section Of Physics Letters* **377**, 81–279 (2003).

[18] Jung, G., Savo, B. & Yuzhelevski, Y. Quiet and noisy metastable voltage states in high-t-c superconductors. *Physical Review B* **62**, 6674–6680 (2000).

[19] Yuzhelevski, Y., Yuzhelevski, M. & Jung, G. Random telegraph noise analysis in time domain. *Review Of Scientific Instruments* **71**, 1681–1688 (2000).

[20] Giusi, G., Crupi, F. & Pace, C. An algorithm for separating multilevel random telegraph signal from 1/f noise. *Rev Sci Instrum* **79**, 024701 (2008).

A Derivations of Formulas

A.1 Proportionality of $\delta \log G$ and $\frac{\delta G}{\langle G \rangle}$

Assume a distribution of $\log G$ with center $\langle \log G \rangle$ and fluctuation amplitude (standard deviation) $\delta \log G \ll 1$:

$$\delta \log G \equiv \sigma_{\log G} \tag{A.1}$$

In linear scale, this translates to an amplitude of:

$$\begin{aligned}
\delta G &= \frac{1}{2} \cdot \left(10^{\langle \log G \rangle + \delta \log G} - 10^{\langle \log G \rangle - \delta \log G} \right) && \text{(A.2)} \\
&= \frac{1}{2} \cdot 10^{\langle \log G \rangle} \left(10^{\delta \log G} - 10^{-\delta \log G} \right) && \text{(A.3)} \\
&= \frac{1}{2} \cdot \underbrace{10^{\langle \log G \rangle}}_{\approx \langle G \rangle} \cdot \underbrace{\left(e^{\delta \log G \ln 10} - e^{-\delta \log G \ln 10} \right)}_{\approx 2\delta \log G \ln 10,\ \delta \log G \ln 10 \ll 1} && \text{(A.4)} \\
&\approx \frac{1}{2} \cdot \langle G \rangle \cdot 2\delta \log G \ln 10 && \text{(A.5)}
\end{aligned}$$

This leads to a relative amplitude of:

$$\frac{\delta G}{\langle G \rangle} = \ln 10 \cdot \delta \log G \tag{A.6}$$

A.2 Autocorrelation Function of a Two-Level Random Telegraph Signal

Definition of autocorrelation:

$$R_{xx}(\Delta t) = \lim_{T \to \infty} \frac{1}{T} \int_0^T x(t) \cdot x(t + \Delta t)\, dt \tag{A.7}$$

We assume a perfect RTS $x(t)$ with two possible values a and b. The two states have average lifetimes τ_a and τ_b while the individual lifetimes are exponentially distributed (constant probability of decay during a unit of time). This means that the values a and b occur with probabilities of $w_a = \frac{\tau_a}{\tau_a + \tau_b}$ and $w_b = \frac{\tau_b}{\tau_a + \tau_b}$, respectively.

Average value:

$$\langle x \rangle = \frac{\tau_a a + \tau_b b}{\tau_a + \tau_b} \tag{A.8}$$

Consider the quantities a' and b' offset by the average ($x' = x - \langle x \rangle$):

$$a' = a - \langle x \rangle = \frac{\tau_b (a - b)}{\tau_a + \tau_b} \tag{A.9}$$

$$b' = b - \langle x \rangle = \frac{\tau_a (b - a)}{\tau_a + \tau_b} \tag{A.10}$$

The value $x'(t + \Delta t)$ can either be equal to $x'(t)$ or not, depending on whether there have been an even or odd number of switching events during Δt. This leads to the following two possible average values for $x'(t) \cdot x'(t + \Delta t)$:

Even number of switches:

$$\begin{aligned} \langle x'(t) \cdot x'(t + \Delta t) \rangle &= w_a \cdot a'^2 + w_b \cdot b'^2 \\ &= \frac{\tau_a}{\tau_a + \tau_b} \cdot a'^2 + \frac{\tau_b}{\tau_a + \tau_b} \cdot b'^2 \\ &= \frac{\tau_a}{\tau_a + \tau_b} \left(\frac{\tau_b (a - b)}{\tau_a + \tau_b} \right)^2 + \frac{\tau_b}{\tau_a + \tau_b} \left(\frac{\tau_b (a - b)}{\tau_a + \tau_b} \right)^2 \\ &= \frac{\tau_a \tau_b}{\tau_a + \tau_b} \left(\frac{\tau_b (a - b)^2 + \tau_a (a - b)^2}{(\tau_a + \tau_b)^2} \right) = \frac{\tau_a \tau_b (a - b)^2}{(\tau_a + \tau_b)^2} \end{aligned} \tag{A.11}$$

Odd number of switches:

$$\begin{aligned} \langle x'(t) \cdot x'(t + \Delta t) \rangle &= w_a \cdot a' b' + w_b \cdot b' a' \\ &= \frac{\tau_a}{\tau_a + \tau_b} \cdot a' b' + \frac{\tau_b}{\tau_a + \tau_b} \cdot b' a' \\ &= \frac{\tau_a}{\tau_a + \tau_b} \cdot \frac{\tau_b (a - b) \tau_a (b - a)}{(\tau_a + \tau_b)^2} + \frac{\tau_b}{\tau_a + \tau_b} \cdot \frac{\tau_a (b - a) \tau_b (a - b)}{(\tau_a + \tau_b)^2} \\ &= \frac{-\tau_a \tau_b (a - b)^2}{(\tau_a + \tau_b)^2} \end{aligned} \tag{A.12}$$

We notice that the two values are identical except for the sign.

The two decay constants τ_a^{-1}, τ_b^{-1} lead to an average decay constant:

$$\tau^{-1} = \frac{\tau_a^{-1} + \tau_b^{-1}}{2} \tag{A.13}$$

Probability of observing m switching events during time interval Δt (Poisson distribution):

$$P(m, \Delta t) = \frac{\left(\Delta t \tau^{-1}\right)^m}{m!} e^{-\Delta t \tau^{-1}} \tag{A.14}$$

Inserting the possible average conductance values into a sum over all possible numbers of switching events leads to the final autocorrelation function:

$$
\begin{aligned}
R_{xx}(\Delta t) &= \frac{\tau_a \tau_b (a-b)^2}{(\tau_a+\tau_b)^2}\left(\sum_{m=0}^{\infty}(-1)^m P(m,\Delta t)\right) + \langle x\rangle^2 \\
&= \frac{\tau_a \tau_b (a-b)^2}{(\tau_a+\tau_b)^2} e^{-\Delta t \tau^{-1}} \cdot \underbrace{\sum_{m=0}^{\infty}\frac{\left(-\Delta t \tau^{-1}\right)^m}{m!}}_{=e^{-\Delta t \tau^{-1}}} + \langle x\rangle^2 \\
&= \frac{\tau_a \tau_b (a-b)^2}{(\tau_a+\tau_b)^2} e^{-2\Delta t \tau^{-1}} + \langle x\rangle^2 \\
&= \underline{\frac{\tau_a \tau_b (a-b)^2}{(\tau_a+\tau_b)^2} e^{-\Delta t\left(\tau_a^{-1}+\tau_b^{-1}\right)} + \left(\frac{\tau_a a+\tau_b b}{\tau_a+\tau_b}\right)^2}
\end{aligned}
\tag{A.15}
$$

We have not directly shown why the offset is $\langle x\rangle^2$ but it is obvious that in the limit $\Delta t \to \infty$:

$$
\begin{aligned}
\lim_{\Delta t\to\infty} R_{xx}(\Delta t) &= \left(\frac{\tau_a}{\tau_a+\tau_b}\right)^2 \cdot a^2 + \left(\frac{\tau_b}{\tau_a+\tau_b}\right)^2 \cdot b^2 + 2 \cdot \left(\frac{\tau_a}{\tau_a+\tau_b}\right)\left(\frac{\tau_b}{\tau_a+\tau_b}\right) \cdot ab \\
&= \left(\frac{\tau_a a+\tau_b b}{\tau_a+\tau_b}\right)^2
\end{aligned}
\tag{A.16}
$$

B Additional Data

B.1 Alkane Measurements

Figure B.1 shows histograms for alkanedithiols obtained from more opening curves. The most probable conductance values plotted against the number of carbon atoms fit an exponential decay quite well (figure B.2).

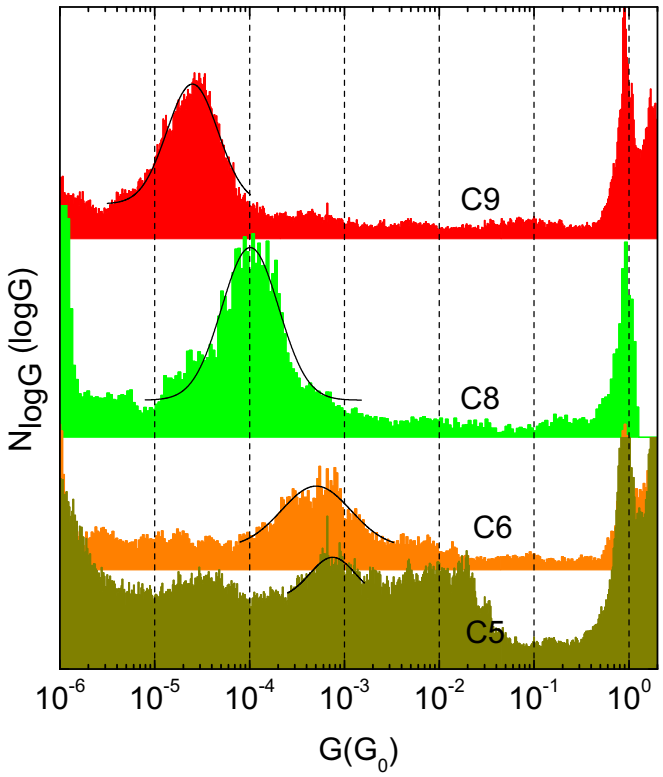

FIGURE B.1: Conductance histograms of alkanedithiols from 344 curves (C9), 100 curves (C8), 160 curves (C6) and 720 curves (C5).

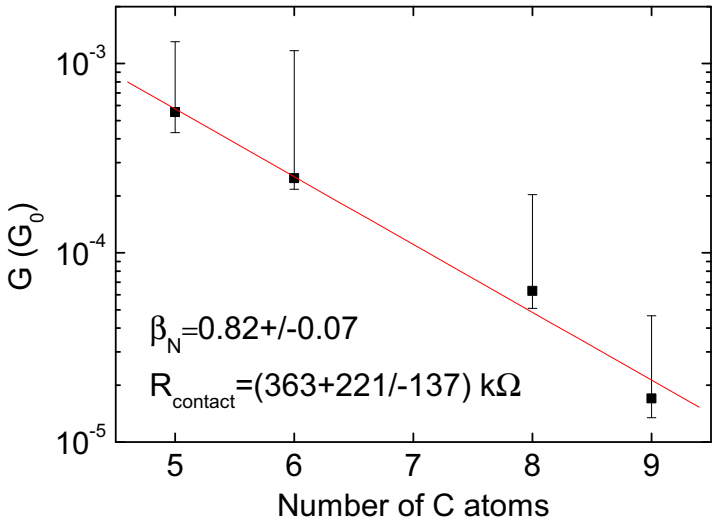

FIGURE B.2: Linear fit to the logarithms of the conductance values obtained from the histograms.

B.2 Table of Decay Constants

molecule	sample	γ	$\langle \delta \log G \rangle$	$\sigma_{\delta \log G}$	number of measurements
mesitylene	08b	0.19	0.031	0.017	2
mesitylene	10a	0.10	0.024	0.013	6
C8	06b	0.22	0.060	0.055	10
C8	08b	0.25	0.047	0.046	13
C8	13a	0.25	0.046	0.064	4
C8	15a	0.30	0.048	0.069	10
C8	15b	0.13	0.034	0.021	4

TABLE B.1: Slopes γ showing the dependence of the fluctuation amplitude $\delta \log G$ on the average conductance $\langle G \rangle$ for different measurements in mesitylene and C8. Also, the average fluctuation amplitude $\langle \delta \log G \rangle$ and their standard deviation $\sigma_{\delta \log G}$ is shown for each sample.

B.3 Bandwidth of Setup

To obtain the bandwidth of the setup, the thermal current noise of different resistors was measured through the IV converter for the two gain settings used in fixed position measurements (10^9 V/A and $0.22 \cdot 10^8$ V/A) with a sampling rate of 100 kHz. Figure B.3 shows the spectra averaged from 100 1 s measurements. The amount of noise matches well the expected current noise power density of $\overline{I_{R,eff}} = \sqrt{4k_BT/R}$ indicated as solid horizontal lines. For a high resistance, the upper frequency limit is at approximately

1.3 kHz for a gain of 10^9 V/A and 10 kHz for a gain of $0.22 \cdot 10^8$ V/A (−3 dB values indicated by dashed lines).

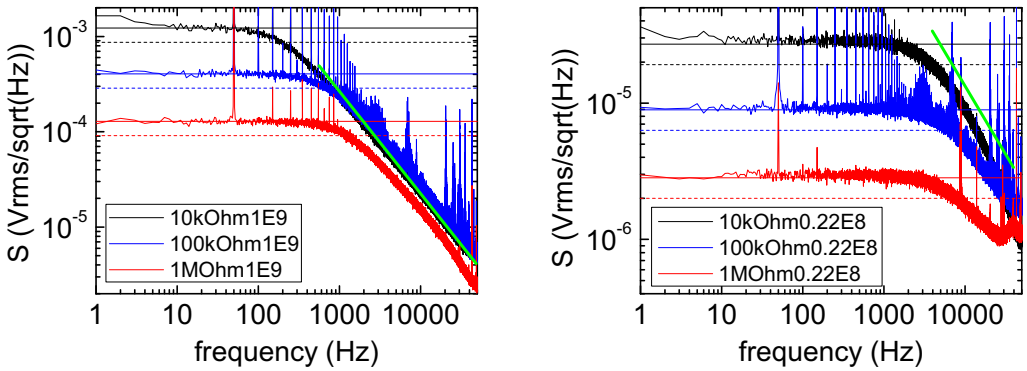

FIGURE B.3: Thermal current noise of three different resistors measured through to the IV converter for the two different gain settings used in the fixed position measurements. It can be seen that for large resistance, the bandwidth of the setup is limited to approximately 1300 Hz for a gain of 10^9 V/A (left) and 10 kHz for a gain of $0.22 \cdot 10^8$ V/A (right). The green lines correspond to a first order low pass (1/f), the horizontal lines indicate the expected thermal noise (solid) of the resistors and the −3 dB values thereof (dashed).